Identifying the most (cost-)efficient regions for CO_2 removal with Iron Fertilization in the Southern Ocean

Short title: (Cost-)efficiency of Southern Ocean Iron Fertilization

Lennart T. Bach[1]*, Veronica Tamsitt[2], Kimberlee Baldry[1], Jeffrey McGee[1,3], Emmanuel C. Laurenceau-Cornec[1,4], Robert F. Strzepek[1,5], Yinghuan Xie[1], Philip W. Boyd[1,5]

[1]Institute for Marine and Antarctic Studies, University of Tasmania, Hobart, Tasmania, Australia.
[2]College of Marine Science, University of South Florida, St Petersberg, Florida, USA.
[3]Faculty of Law, University of Tasmania, Hobart, Tasmania, Australia.
[4]Univ. Brest, CNRS, IRD, Ifremer, LEMAR, Plouzane, France.
[5]Australian Antarctic Program Partnership, Hobart, Tasmania, Australia.
*Corresponding Author: lennart.bach@utas.edu.au

Key Points

- Iron fertilization efficiency is constrained mainly by carbon transfer efficiency into Antarctic Bottom Water and air-sea CO_2 exchange.
- Iron fertilization could cost below 100 US-Dollar per tonne CO_2 on Antarctic shelves but may be much more expensive off shelves.
- (Cost-)efficient Iron Fertilization is restricted to relatively small parts of the Southern Ocean that are protected by international law.

Abstract

Ocean Iron Fertilization (OIF) aims to remove carbon dioxide (CO_2) from the atmosphere by stimulating phytoplankton carbon-fixation and subsequent deep ocean carbon sequestration in iron-limited oceanic regions. Transdisciplinary assessments of OIF have revealed overwhelming challenges around the detection and verification of carbon sequestration and wide-ranging environmental side-effects, thereby dampening enthusiasm for OIF. Here, we utilize 5 requirements that strongly influence whether OIF can lead to atmospheric CO_2 removal (CDR): The requirement (1) to use preformed nutrients from the lower overturning circulation cell; (2) for prevailing Fe-limitation; (3) for sufficient underwater light for photosynthesis; (4) for efficient carbon sequestration; (5) for sufficient air-sea CO_2 transfer. We systematically evaluate these requirements using observational, experimental, and numerical data to generate circumpolar maps of OIF (cost-)efficiency south of 60°S. Results suggest that (cost-)efficient CDR is restricted to locations on the Antarctic Shelf. Here, CDR costs can be <100 US$/tonne CO_2 while they are mainly >>1000 US$/tonne CO_2 in offshore regions of the Southern Ocean, where mesoscale OIF experiments have previously been conducted. However, sensitivity analyses underscore that (cost-)efficiency is in all cases associated with large variability and are thus difficult to predict, which reflects our insufficient understanding of the relevant biogeochemical and physical processes. While OIF implementation on Antarctic shelves appears most (cost-)efficient,

it raises legal questions because regions close to Antarctica fall under 3 overlapping layers of international law. Furthermore, the constraints set by efficiency and costs reduce the area suitable for OIF, thereby likely reducing its maximum CDR potential.

1. Introduction

Restricting global warming to 1.5°C requires atmospheric carbon dioxide (CO_2) removal of 100-1000 gigatonnes (Gt) until 2100 as a supplement to rapid emissions reduction (Rogelj et al. 2018). It has been proposed that Gigatonne-scale CO_2 removal (CDR) will be realized by using a portfolio of methods, but they generally lack technological readiness (Nemet et al. 2018). Ocean Iron Fertilization (OIF) is a widely considered method within the marine CDR portfolio. OIF aims to stimulate CO_2 fixation by marine phytoplankton through the addition of dissolved iron to nutrient-rich (nitrate, phosphate) but iron-limited surface ocean regions, mainly in the Southern Ocean or in low iron regions of the Pacific Ocean. The rationale for CDR is that a significant proportion of the additional CO_2 fixed in phytoplankton biomass will then sink into the deep ocean, where the carbon (C) could be sequestered for centuries to millennia (Martin 1990). Indeed, paleo-oceanographic evidence suggests that changes in iron delivery to the surface ocean via dust and the associated enhancement of deep ocean CO_2 sequestration could explain around 25% of the 80 ppmv glacial-interglacial atmospheric CO_2 transitions (Martínez-García et al. 2014).

Research into OIF commenced in the 1980's and was largely informed by 13 mesoscale iron fertilization experiments (Yoon et al. 2018), which aimed to answer fundamental questions in climate science (Martin 1990). Today, OIF is arguably the most thoroughly assessed marine CDR method, having undergone scrutiny by transdisciplinary international research efforts. The early enthusiasm for OIF faded with increasing understanding of the complexity of the method and growing concerns around environmental side-effects (de Baar et al. 2005; Strong et al. 2009; Buesseler 2012; Gattuso et al. 2018; Rohr 2019). However, despite justified skepticism, OIF is still considered as a potential addition to the CDR portfolio needed to achieve net zero goals (Fuss et al. 2018) and there is renewed interest in large-scale scientific assessment of this CDR method (NASEM 2021; Buesseler et al. 2023).

Simulations with biogeochemical models project that continuous basin-scale or globally-applied OIF could sequester around 2-4 Gt CO_2 $year^{-1}$ (Aumont and Bopp 2006; Zahariev et al. 2008; Oschlies et al. 2010; Fu and Wang 2022). However, OIF would likely not be achievable at such a large scale due to environmental concerns, associated legal constraints and hence difficulties in obtaining social license (Strong et al. 2009; Cox et al. 2021). Indeed, the same modeling studies have highlighted negative side-effects of large scale and continuous Southern Ocean OIF deployments, such as so-called 'nutrient robbing' by OIF upstream (i.e., poleward in the Southern Ocean) from low-latitude regions, water column deoxygenation, and the formation of more potent greenhouse gasses in oxygen-depleted waters (Aumont and Bopp 2006; Zahariev et al. 2008; Oschlies et al. 2010; Fu and Wang 2022). Furthermore, the outcomes of some model simulations have suggested that targeting particular regions or seasons could optimize the CDR efficiency of OIF (Gnanadesikan et al. 2003; Arrigo and Tagliabue 2005; Gnanadesikan and Marinov 2008; Sarmiento et al. 2010; Fu and Wang 2022). For example, Sarmiento et al (2010) simulated OIF at two sites in the Pacific and two sites in the Southern Ocean. They found substantially higher CDR efficiencies in the Southern Ocean,

in particular in the Ross Sea (Sarmiento et al. 2010). Their findings suggest that OIF would more likely become a meaningful addition to the global CDR portfolio when deployed in locations of the Southern Ocean where its CDR efficiency (i.e., CDR per added iron) and cost efficiency (i.e., costs per tonne (t) CO_2 removed) is highest and detrimental environmental impacts are minimized. Our study builds upon this previous modeling research and aims to refine our understanding of Southern Ocean Iron Fertilization by providing a spatially resolved circumpolar analysis of CDR- and cost-efficiency.

After the methods section, we begin by evaluating five requirements that largely determine the efficiency of OIF (section 3.1.) and their implications for the maximum CDR potential of OIF (section 3.2.) . Next, we present maps of CDR efficiency and OIF costs in the Southern Ocean south of 60°S (section 3.2.) and discuss the variability of OIF (cost-)efficiency (section 3.4.). Last, we discuss the legal ramifications (section 3.5.) and synthesize the key findings of this study (section 4).

2. Methods

2.1. Iron limitation south of 60°S

To determine the onset of iron-limitation for phytoplankton communities south of 60°S, we synthesized published shipboard iron-amendment experiments using the following search query on Google Scholar (31, July 2019): "phytoplankton" OR "microalgae" OR "algae" OR "diatom" OR "Phaeocystis" AND "iron" AND "growth" AND "Southern Ocean" OR "Antarctic" OR "Antarctica". The first 200 hits were inspected. Relevant datasets were those where natural communities from south of the polar front were incubated under iron-replete (+Fe) and iron-deplete (-Fe) conditions and growth rates from both treatments, as well as background dissolved iron (DFe) concentrations were reported (Table S1). An additional search with the same query but restricting the search to papers published since 2015 was done afterwards because there was a bias towards older and more frequently cited literature.

Growth rates (μ) were calculated from chlorophyll a (chla) increase, particulate organic carbon (POC) accumulation, or nitrate draw-down. In some studies growth rates were not provided as numbers but had to be calculated using the following equation:

$$\mu = \frac{ln\,(t_{end}) - ln\,(t_{start})}{d} \qquad (1)$$

where t_{start} and t_{end} is chla or POC concentration at the start and the end of the experiment, respectively and d is the duration of the experiment in days. (Please note that it was $\ln(t_{start})$-$\ln(t_{end})$ in the numerator of equation 1 in calculations using nitrate drawdown.). For this calculation, data often (especially in the older literature) needed to be extracted from plots using the data grabbing tool WebPlotDigitizer (https://automeris.io/WebPlotDigitizer/). We calculated the fold change of growth rate and plotted μ_{+Fe}/μ_{-Fe} as a function of the *in situ* background (i.e. pre-treatment) DFe concentration from the batch of seawater which was incubated. Bioavailability of DFe was not considered as this was seldom reported in the literature.

2.2. Phytoplankton light limitation south of 60°S

We applied the observation-based approach of Venables and Moore (2010) to assess if light could limit phytoplankton growth during summer south of 60°S. Satellite and Argo float data were used to calculate the mean irradiance in the surface mixed layer (I_{MLD}) and compare this to the threshold irradiance above which phytoplankton communities can grow (I_{MLD_min}).

I_{MLD} (mol photons m^{-2} d^{-1}) was calculated as:

$$I_{MLD} = \frac{PAR_{belowsurf}}{K_d h}(1 - e^{-K_d h}) \quad (2)$$

where $PAR_{belowsurf}$ is the photosynthetically active radiation (PAR) just below the sea surface (mol photons m^{-2} d^{-1}), K_d the diffuse downwelling attenuation coefficient (m^{-1}), and h the mixed layer depth (m). Downwelling $PAR_{belowsurf}$ is lower than PAR above the surface ($PAR_{abovesurf}$) because part of the sunlight is reflected at the sea surface. The reflected fraction at the air-sea interface depends on a range of factors such as sun zenith angle, wind speed, or cloud cover (Campbell and Aarup 1989; Mobley and Boss 2012). Between 60 – 70°S, reflection is approximately 7% for clear sky conditions and calm water during summer (less reflection for wind speed >0 m/s and overcast sky (Campbell and Aarup 1989; Mobley and Boss 2012). Sea ice is another medium that absorbs light before it can enter the ocean. Light absorption by sea ice depends on snow cover or the presence of melt ponds on ice but was shown to be on average 0.957 (mean transmission = 0.043) (Katlein et al. 2019). Using this information, we approximated $PAR_{belowsurf}$ as:

$$PAR_{belowsurf} = PAR_{abovesurf} * (0.07 * IC + 0.93) * (1 - IC * 0.957) \quad (3)$$

where IC is the sea ice cover from 0 (no ice) to 1 (complete coverage). This equation balances the influence of reflection of PAR at the liquid air-sea interface and the absorption of PAR by sea ice within a grid field.

K_d was estimated from satellite chlorophyll a following (Venables and Moore 2010):

$$K_d = 0.05 + 0.057 * chla^{0.58} \quad (4)$$

where chla is the chlorophyll a concentration in mg m^{-3}. $PAR_{abovesurf}$, IC, and chla were obtained from the NASA Giovanni online data system. More specifically, we downloaded gridded data of austral summer averages (December-February (DJF) 2010-2020) of "photosynthetically available radiation (MODISA_L3m_PAR v2018)" and "Sea-ice covered fraction of tile (M2TMNXFLX v5.12.4)" from the MERRA-2 Model, and "Chlorophyll a concentration (MODISA_L3m_CHL v2018)" from the MERRA-2 Model.

We used an Argo-based climatology to obtain mean DJF mixed layer depths (h) for south of 60°S (Holte et al. 2017). Spatial resolution differed between $PAR_{abovesurf}$, chla (both 1/24 degree), IC (0.5 x 0.625 (lat x lon) degree), and h (0.5

degree), so that they were re-gridded to 0.5 degrees using raster functions and bilinear interpolation with the software R. Mixed layer depth, as well as K_d, IC, and $PAR_{belowsurf}$ are shown in Fig. S1.

Venables and Moore (2010) determined an I_{MLD_min} of 3 mol photons m^{-2} d^{-1} in the Southern Ocean by comparing I_{MLD} in Fe-limited regions with I_{MLD} in naturally Fe-fertilized regions (e.g. near the Kerguelen Islands). To further constrain I_{MLD_min}, we explored the literature for growth vs. irradiance curves with Southern Ocean phytoplankton species. Our goal was to approximate the daily irradiance above which growth rates are saturated. The reason why we specifically looked for growth rates and not photosynthesis rates is that growth rates are measured over days to weeks while photosynthesis rates are usually measured for hours. Thus, phytoplankton can be assumed to be acclimated to the light levels they are exposed to during the incubation. To find relevant studies we used Google Scholar (29 April 2020) and searched for: "Light" OR "Irradiance" OR "radiation" AND "Southern Ocean" AND "phytoplankton". We only found 2 relevant studies in the first 100 hits so we looked more specifically into the reference lists of these 2 studies and found another 2. We normalized growth rates at each light level to the maximum growth rate measured within a growth vs. irradiance curve (Table S2). Finally, we fitted a growth vs. irradiance model (Eilers and Peeters 1988) to the binned data to determine the irradiance that corresponds to the onset of irradiance saturation. The data also suggest the potential for light inhibition at high irradiance but this aspect is not considered in our study as it may reduce growth rates but is unlikely to stop growth (i.e. growth rates remained positive in the data compiled at high irradiance).

2.3. Virtual particle tracking in a high-resolution physical ocean model

We used output from MOM01 (Morrison et al. 2020), an ocean sea-ice model based on version 5 of the Modular Ocean Model (MOM) code (Griffies 2012) for several specific aspects addressed in this study. The model has 1/10 degree horizontal resolution and 75 vertical levels extending over the full ocean depth, with vertical resolution in the top 1000 m ranges from 1.1 m at the surface to 94 m at 1000 m depth. The atmospheric forcing is derived from version 2 of the Coordinated Ocean-ice Reference Experiments - Normal Year Forcing (CORE-NYF) reanalysis (Large and Yeager 2009). Sea surface salinity is restored to a seasonally varying climatology on a 60 day timescale with a piston velocity of 0.16 m day^{-1}. The model does not include ice shelf cavities or tides, and glacial meltwater is input at the sea surface. The model was spun up for 80 years with repeated annual forcing, and then 10 years of daily averaged output was saved for analysis.

We conducted a virtual particle tracking experiment using the Connectivity Modeling System Lagrangian code (CMS, (Paris et al. 2013)) with daily averaged three-dimensional velocity fields from the first year of MOM01 output. In our simulation, 238221 neutrally-buoyant virtual particles were seeded on January 3rd at 0.5 m depth in each model horizontal grid box south of 60°S and advected forward in time for one year with the MOM01 velocity fields. Particles were advected with a timestep of 90 minutes using a 4th order Runge-Kutta scheme to calculate particle advection, applied in both space and time and particles were reflected at topography or the sea surface. Particle trajectory positions were saved every 5 days and MOM01 temperature and salinity fields saved along each particle trajectory. We note that the velocity fields used for advecting the particles do not explicitly include mixed layer convection or interior diffusive mixing processes, which affect the movement of tracers. This is a limitation of the chosen method,

however running online Eulerian tracer releases in the model is prohibitively expensive. We further discuss the potential implications of this limitation on the results of the particle tracking experiment in Section 3.1.4.

First, we utilized particle trajectories to explore the potential for export of neutrally buoyant OIF-derived carbon (e.g., dissolved organic carbon or suspended POC) via physical downwelling. Physical downwelling was considered to be successful if particles reached a potential density referenced to 1000 m >32.56, representative of Dense Shelf Waters, and also reached a depth of ≥750m within one year of simulation (Fig. S2). Second, we utilized particle trajectories to estimate how far particles drift horizontally from the release location within one month of simulation (see Fig. S3 for details). Third, we used particle trajectories (and other model output from MOM01) for the calculations of air-sea CO_2 exchange as explained in detail below.

2.4. Equilibration of OIF-derived seawater CO_2 deficit with atmospheric CO_2

There is a risk that OIF reduces CO_2 concentrations in seawater but the water parcel carrying this CO_2 deficit subducts below the sea surface before CO_2 equilibration with the atmosphere has been completed. In such a case, atmospheric CO_2 removal is delayed potentially far into the future when the CO_2-deficient water is re-exposed to the atmosphere (He and Tyka 2023). To investigate this risk, we simulated a Lagrangian experiment for the temporal evolution of a 35 μmol kg^{-1} deficit in dissolved inorganic carbon (DIC), which is conceptually illustrated and outlined in Fig. 1. A 35 μmol kg^{-1} DIC deficit is typical of OIF experiments with shallow mixed layers of ~40 m during summer (de Baar et al. 2005; Krishnamurthy et al. 2008) and is equivalent to a 35 μmol/kg CO_2 deficit when alkalinity remains unchanged. A water parcel carrying the CO_2 deficit is represented by the trajectories of neutrally-buoyant virtual particles released in January from MOM01 (section 2.3). The CO_2-deficient water parcels spread horizontally (following the virtual particle trajectories) and can exchange CO_2 with the atmosphere for as long as the particles are in the mixed layer. Hence, these CO_2-deficient water parcels can be thought of as "buckets", which are initially empty and can fill up with maximally 35 μmol/kg atmospheric CO_2 until the bucket is full (Fig. 1A).

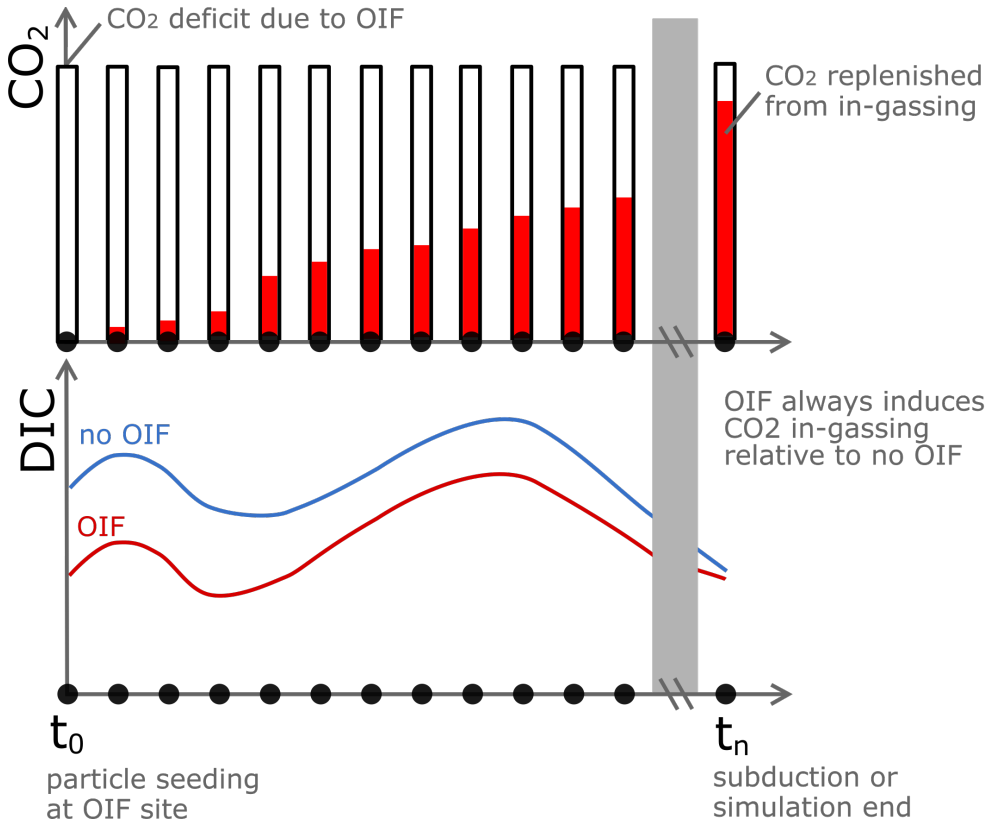

Figure 1. Conceptual framework of the air-sea CO_2 equilibration calculation. (**A**) Representation of the "bucket" approach. The initial DIC deficit (equivalent to a seawater CO_2 deficit) of 35 µmol/kg gradually (white bar) fills up with atmospheric CO_2 (red bar) over time until the water parcel carrying the deficit subducts below the mixed layer. The extent to which the bucket is full at the time of exiting the mixed layer (f_{Eq}) is the target variable of this calculation. (**B**) Representation of the background biogeochemical state of DIC (no OIF scenario; blue line) and how a hypothetical OIF operation which generated a 35 µmol/kg DIC deficit (red line) approaches the background state over time through atmospheric CO_2 influx. Strengths and weaknesses of this approach are discussed in section 3.1.5.

Air-sea CO_2 influx into the "buckets" is calculated along their trajectories using climatological data (Table S3). We compare the air-sea CO_2 exchange in an unperturbed "no-OIF scenario" with the exchange in an "OIF scenario" where 35 µmol/kg DIC were subtracted from the gridded DIC climatology (Fig. 1B). In the calculation, the no-OIF scenario is the expected biogeochemical state along the particle trajectory. The no-OIF scenario allows us to account for changes in air-sea gas exchange due to expected background changes in the carbonate system (i.e., variability in water mass mixing, sea-ice changes and biology). The OIF scenario is the alternate state along a particle trajectory representing an initial DIC deficit of 35 µmol kg^{-1} following OIF and the subsequent change caused by CO_2 exchange with the atmosphere (Fig. 1B). In the OIF scenario, the DIC perturbation (DIC_{ptb}) cumulatively changes along a particle trajectory according to the amount of DIC that has been added to the system by air-sea gas exchange and always exhibits a CO_2 influx relative to the no-OIF scenario (i.e. the background biogeochemical state). This is represented as:

$$DIC_{ptb}\ (t > 0) = 35 - \sum_{t=0}^{n-1} \quad (\Delta DIC'(t) - \Delta DIC(t)) \qquad (5)$$

where $DIC_{ptb}(t=0)$ is 35 µmol kg^{-1}, **Δ**DIC(t) is the DIC added to the system over 5 days due to air-sea gas exchange of the expected biogeochemical state at timestep t, and **Δ**DIC'(t) is the DIC added to the system over 5 days due to air-sea gas exchange of the perturbed system at timestep t.

To derive DIC_{ptb}, consider the derivation of ***Δ***DIC from air-sea fluxes for the no-OIF and the OIF scenarios. ***Δ***DIC is calculated by first calculating air-sea CO_2 flux (F) over the mixed layer.

$$F = G \times K_0 \times (pCO_{2\_SW} - pCO_{2\_air}) \qquad (6)$$

where G is the gas-exchange constant (m s^{-1}), K_0 is the solubility constant (mol m^{-3} atm^{-1}), pCO_{2_SW} is the partial pressure of CO_2 in seawater (µatm) and pCO_{2_air} is the partial pressure of CO_2 in air (µatm). Then ***Δ***DIC (µmol kg^{-1}) can subsequently calculated by iteratively integrating F over 5 days

$$\Delta DIC = \frac{F \times t}{h \times \rho} \qquad (7)$$

where t is 5 days (s), ***ρ*** is the density of seawater (kg m^{-3}) calculated from salinity and temperature using seacarb (Gattuso et al. 2021), h is the mixed-layer depth (m) from MOM01.

Thus to calculate DIC*_ptb*, equation (5) should be expanded using equations (6) and (7) with the assumption that atmospheric pCO_2 remains unchanged between the two scenarios.

$$DIC_{ptb}(t > 0) = 35 + \sum_{t=0}^{n-1} \frac{G(t) \times K_0 \times t}{h(t) \times \rho(t)} (pCO'_{2\_SW}(t) - pCO_{2\_SW}(t)) \qquad (8)$$

The gas exchange constant (G) was calculated using daily mean climatologies of wind speed, temperature and salinity (Table S3) according to Wanninkhof (2014). We linearly scaled G to sea-ice concentration (Butterworth and Miller 2016; Prytherch et al. 2017). The solubility constant (K_0) was calculated using the fourth order polynomial of Wanninkhof (2014). MOM01 model mixed layer depth (h) and the density of seawater (ρ) was calculated from salinity and temperature (Table S3) using the function "rho" from the R "seacarb" package (Gattuso et al. 2021).

To calculate $pCO'_{2\_SW}(t)$ and the carbonate system at the alternate state, we calculated perturbed DIC (DIC'(t)) at each time step using the expected DIC from the no-OIF scenario (DIC(t)) and the amount of DIC added by air-sea gas exchange due to the OIF deficit (DIC_{ptb}):

$$DIC'(t) = DIC(t) - DIC_{ptb}(t) \qquad (9)$$

where DIC(t) was calculated from 1x1 monthly mean climatologies and modeled alkalinity (from the Locally Interpolated Alkalinity Regression v2, (Carter et al. 2018)) using the "carb" function in the R package "seacarb" (Gattuso et al. 2021) with K1 and K2 constants from Millero et al. (2006). DIC'(t) was then used to calculate the

perturbed pCO_2 of the seawater pCO_2'_SW at each time-step (Millero et al. 2006; Gattuso et al. 2021). We assumed that alkalinity changes are negligible.

Finally, we can calculate the fraction of the DIC deficit that is replenished by atmospheric CO_2 influx (f_{Eq}) at each time-step:

$$f_{Eq} = \left(\frac{1-DIC_{ptb}}{35}\right) \quad (10)$$

We only calculated fEq where sea-ice concentration was <60%. This minimized the amount of missing data within our calculations and allowed more trajectories to be included in our analysis, but underestimates CO_2 in-gassing over time under sea-ice, as gas exchange is expected to vary linearly with sea-ice concentration (Butterworth and Miller 2016; Prytherch et al. 2017). The OIF scenario was considered fully equilibrated when $DIC_{ptb} \leq 0$, converging to the no-OIF scenario (Fig. 1B).

2.5. Estimates of CO_2 removal using OIF

We refined an equation originally derived by Harrison (2013) to estimate how much of the CO_2 fixed by phytoplankton is transferred into AABW and can be considered as CDR in t C km^{-2} for time-scales of AABW re-ventilation to the atmosphere (i.e. likely >>100 years (England 1995; Siegel et al. 2021)). This equation is composed of 5 components (I-V), introduced in the 5 following paragraphs and combined into one equation thereafter.

Component I estimates the POC build-up (t C km^{-2}) within a patch of water after iron fertilization:

$$POC = 1.5 \times MLD \times C/Fe \times \frac{12}{1000000} \quad (11)$$

Based on previous *in situ* experiments we assume that OIF increases DFe by 1.5 nM above background concentrations (de Baar et al. 2005) in a patch of 1 km^2 and a given mixed layer depth (MLD) in meters. POC in this patch then depends on the carbon-to-iron molar elemental ratio (C/Fe) of phytoplankton organic matter, which we assumed to be 25,000 (Twining et al. 2004; de Baar et al. 2005) to reduce the risk of overestimating the CDR potential of OIF. The factor 12/1000000 is used to calculate the mass of carbon, where 12 is the molecular weight in g mol^{-1} and 1000000 is to bring the term to the unit t C km^{-2}. Please note that we neglect the formation of dissolved organic carbon (DOC) here as another aspect of our analysis suggested rather limited success of DOC being entrained in forming deep-water (section 3.1.4). However, when (apparently low) fractions of produced DOC are entrained into AABW, they make OIF more efficient and reduce costs.

Component II estimates how much of the POC produced in the surface (eq. 11) reaches a certain depth (z). The fraction of POC reaching a depth ≥100 m (POC_z) was estimated with a power-law function:

$$POC_z = POC * e * \left(\frac{z}{100}\right)^{-b} \quad (12)$$

where the export-ratio (e) is the fraction of primary production sinking below 100 m (between 0 and 1), and b determines the degree of flux attenuation (Martin et al. 1987). The export-ratio and b-values have been empirically determined and were compiled from the literature and by using satellite primary production products for the Southern Ocean south of 60°S (see Tables S4 and S5 for further details). The 122 export-ratios ranged from 0.005 – 0.96 with a median of 0.28 (Table S4). The 31 b-values ranged from 0.25-1.97 with a median of 0.96 (Table S5).

POC_{AABW} is the specific case where POC_z is calculated for the surface depth of AABW. This spatially variable depth horizon (Fig. 4F) was chosen as target depth because we consider POC sinking into AABW to be sequestered for relatively long timescales (discussed in section 3.1.4). The depth of the upper interface of the AABW layer was defined here as the time-mean depth of the σ_1=32.56 isopycnal surface in the MOM01 model.

Component III (f_{Seq}) assesses how much of the OIF-derived POC that reaches the AABW surface layer (POC_{AABW}) is matched with the influx of atmospheric CO_2. The rationale for this metric is that not all CO_2 consumed by phytoplankton during the OIF-induced bloom must be matched with atmospheric CO_2 because much of it will be respired in and near the surface within weeks (Boyd et al. 2004). Thus, only the "sequestered" POC fraction (i.e. POC_{AABW}) must be matched as this is the amount of POC accounted for as CDR (see below). f_{Seq} was calculated as:

$$f_{Seq} = f_{Eq} \div \left(\frac{POC_{AABW}}{POC}\right) \qquad (13)$$

Here, $f_{Seq} \geq 1$ means that POC_{AABW} is fully matched with atmospheric CO_2 influx, while any value <1 suggests that air-sea CO_2 has only been partially sequestered (by the fraction between 0 and 1) .

Component IV describes how much of the reduction of radiative forcing through CDR is offset through the production of nitrous oxide (N_2O), a greenhouse gas (a ~300 times more potent greenhouse gas than CO_2) that can be produced following OIF, e.g. via nitrification (Law and Ling 2001). Hence, the formation of N_2O must be considered an offset to CDR:

$$N2O_{offset} = f_{N2O} \times POC \times e \times \left(1 - \left(\frac{z_{AABW}}{100}\right)^{-b}\right) \qquad (14)$$

Here, f_{N2O} is the N_2O offset factor, which was determined to be 0.13 ±0.06 (i.e., 13 ±6% of the CDR generated by OIF needs to be discounted by the N_2O feedback (Jin and Gruber 2003)). The offset was chosen as it was specifically estimated for a Southern Ocean iron fertilization (Jin and Gruber 2003). The dependency on POC sequestration assumes that this discount only needs to be subtracted if the POC is remineralized in a water mass that quickly re-exposes the N_2O to the atmosphere. Thus, no discount occurs when POC reaches AABW where the forming N_2O gas would be sequestered for longer timescales.

Component V ($O_{transport}$) is the CDR offset related to the combustion of fuels for transporting and distributing the iron to the Southern Ocean. It is based on the assumption that a suitable ship for OIF emits ~1.7 t C d^{-1} (Harrison 2013).

Accounting for iron transport and distribution (see following section) yields a value of 0.01 t C km^{-2} of fertilized area (Harrison 2013).

By combining components I-V we yield the following equation to calculate CDR:

$$CDR = POC_{AABW} \times f_{Seq} - N2O_{offset} - O_{transport} \quad (15)$$

The equation was applied to determine spatially resolved CDR as shown in Fig. 5A. Please note that we converted CDR from t C km^{-2} to t CO_2 km^{-2} by multiplication with 3.67.

2.6. Costs of OIF

To estimate OIF costs in \$US t^{-1} CO_2 sequestered in AABW, we first needed to determine operational costs. These were defined as the sum of costs for Fe fertilizers, transport, and distribution in the Southern Ocean.

One operational challenge for OIF is that relatively small amounts of Fe have to be distributed over large areas. Therefore, small vessels are more economical to distribute the Fe within the summer season as larger ships are not fast enough to distribute their load in summer. Following Harrison (2013), we consider a vessel with a payload of 100 t and an optimal speed of 16.7 km h^{-1}. Such a vessel can fertilize 272 km^2 d^{-1} ($fert_{area}$) at operational costs ($costs_{op}$) of 5000 \$US d^{-1} (Harrison 2013) The vessel would need to sail to the fertilization location before and after the OIF operation and need to be restocked for 3 days ($harbor_{time}$). The Fe fertilizer to be used could be iron(II) sulfate heptahydrate which costs 600 \$US t^{-1} ($costs_{Fe}$) (Harrison 2013). The fraction of iron by weight is 0.2 in iron(II) sulfate heptahydrate (Boyd et al., 2000) and the molecular weight (mol_{weight}) of iron is 55.845 g mol^{-1}). The vessel requires a certain amount of time ($fert_{time}$) to enrich the surface mixed layer by $fert_{conc}$ = 1.5 nM, depending on the vessel speed. For our calculation we used a MLD of 32.8 m which is the summer (December-February) average south of 60°S computed from an Argo float climatology (Holte et al. 2017). Under the above circumstances, the fertilized volume ($fert_{volume}$) can be calculated as:

$$fert_{volume} = fert_{area} \times MLD \quad (16)$$

Which is 8.92 km^3 d^{-1} in our scenario. This would require a daily amount of iron fertilizer (Fe_{fert}) 3.74 t d^{-1} calculated as:

$$Fe_{fert} = fert_{volume} \times fert_{conc} \times \frac{mol_{weight}}{0.2}/1000 \quad (17)$$

where 1000 is to convert this to t d^{-1}. Thus, the payload of the ship would be distributed in 27 days ($fert_{time}$) calculated as:

$$fert_{time} = \frac{payload}{Fe_{fert}} \quad (18)$$

With harbor time (3 days) and sailing back and forth 1800 km (distance from Tasmania to 60°S) to the OIF site (~16 days), the entire cycle ($cycle_{time}$) takes 46 days calculated as:

$$cycle_{time} = fert_{time} + habor_{time} + sailing_{time} \quad (19)$$

The costs per fertilized km^2 ($costs_{area}$) are 35 \$US km^{-2} calculated as:

$$costs_{area} = \frac{cycle_{time} \times costs_{op} + (payload \times costs_{Fe})}{fert_{time} \times fert_{area}} \quad (20)$$

In this equation, all added Fe is assumed to become bioavailable. However, previous mesoscale experiments found that considerable but highly variable fractions of added Fe are lost, for example through particle scavenging and sinking (Bowie et al. 2001). To account for this we assumed that 50% of the added iron is lost due to inorganic particle sinking, which is an upper estimate (Bowie et al. 2001). This was implemented by doubling Fe_{fert} (from 3.74 to 7.48 t d^{-1}) in eq. (18), which increased the $costs_{area}$ from 35 to 51 \$US km^{-2}. We further explored the range of operational $costs_{area}$ within the framework of the above calculation by varying some crucial input assumptions ($costs_{op}$, $costs_{Fe}$, fraction of inorganic particle sinking, Table S6). This sensitivity test revealed that $costs_{area}$ range between 39-145 \$US km^{-2} for optimistic to more pessimistic assumptions (Table S6). Finally, the costs of CDR per t of CO_2 sequestered in AABW (\$US t^{-1} CO_2) were calculated as:

$$Costs_{tonne} = \frac{Costs}{CDR} \quad (21).$$

For the spatial analysis of $Costs_{tonne}$, we use intermediate $costs_{area}$ from Table S6, i.e. 74 \$US km^{-2}.

2.7. Variability of carbon export, CDR, and OIF costs

We conducted Monte Carlo simulations to assess the variability in carbon export, CDR, and OIF costs. These simulations are constrained by the available data.

The amount of POC reaching any given depth (POC_z) can be calculated with equation 12. Here, e and b are the sources for variability. To assess the variability of POC_z, we first generated 1000 e-ratios mimicking their positively skewed distribution that was found when plotting the 122 compiled values (Table S4) in a histogram. For this positively skewed distribution we used a Q-Weibull code in R: qweibull(runif(1000), shape=1.7, scale=0.4). Next, we generated 1000 normally distributed b-values mimicking the distribution of the 31 empirically determined b-values (Table S5) as: rnorm(1000, mean=1.006, sd=0.385). The 1000 e-ratios and b-values were randomly combined in equation 12 to yield the distribution of carbon flux attenuation curves as shown in Fig. 4A and the distribution of POC_z at 4 different

depth horizons (Fig. 4B-E). Please note that we set POC in eq. 12 to 100 in these calculations to yield percent values of how much POC is remaining at any given depth.

A systematic assessment for the predominant drivers of variability in CDR was achieved using eq. 15. We first tested which of the components in eq. 12 has the highest capacity to induce variability in CDR. Therefore, we varied each component individually for 1000 hypothetical cases within their data constraint ranges while keeping the other components constant at their mean values. The parameters individually varied were: 1) The C/Fe ratio in phytoplankton with a mean of 25000 (mol:mol) and a range from 15000-50000 based on measurements by Twining et al. (2004); 2) POC_{AABW} based on variability in e and b as explained in the previous paragraph; 3) f_{N2O} with a mean of 0.13 (factorial offset) and a range from 0.07 to 0.21, based on estimates by Jin and Gruber (2003); $O_{transport}$ with a mean offset of 0.044 tonne CO_2 km^{-2} and a range from 0.022-0.066, assuming 0.5-1.5 times more or less fuel-efficient transport, e.g. via technological improvements or the use of less efficient fuels. For C/Fe, f_{N2O} and $O_{transport}$, values varied randomly (1000 cases) within the entire ranges introduced above using a "runif" function in R (e.g. C/Fe = runif(1000, 15000, 50000)). Last, all ranges were combined in one calculation to estimate the variability in CDR when all data-constraint ranges in C/Fe, POC_{AABW}, f_{N2O} and $O_{transport}$ are considered at the same time. Please note that each Monte Carlo simulation was done for four scenarios: with high (1) and low (0.5) f_{Seq} and and for shallow (200 m) and deep (1000 m) surface depth of AABW. These four scenarios shall be illustrative for the different (and non-random) boundary conditions for air-sea CO_2 influx (section 3.4) and AABW surface layer depth on the Antarctic shelves and off the shelves in the open Southern Ocean.

Finally, we estimated variability in CDR costs with eq. 21. Therefore, operational costs (section 2.6) were varied across the range determined in the sensitivity analysis, i.e. randomly with 1000 cases between 39-145 $US km^{-2} (Table S6). This variability in operational cost was then combined in eq. 21 with the variability in CDR costs from the scenario where variability in C/Fe, POC_{AABW}, f_{N2O} and $O_{transport}$ are considered at the same time.

2.8. Assessment of legal constraints

Different international treaties, including those of the Antarctic Treaty System, could affect the implementation of OIF in the Southern Ocean south of 60°S. We reviewed these treaties using international legal analysis to reveal those that explicitly or implicitly consider OIF. The regions for which these treaties apply were subsequently mapped to illustrate where in the Southern Ocean legal challenges can be expected (see Figure 8).

3. Results and discussion

3.1. Five requirements for the (cost-)efficiency of OIF in the Southern Ocean

In the following 5 subsections (3.1.1. - 3.1.5.), we discuss 5 requirements that should be met to make OIF more (cost-)efficient. We outline why these requirements are important and we assess where in the Southern Ocean they are likely to be met. Please note that the selection of requirements is meant to cover predominant factors influencing OIF (cost-

)efficiency, based on our presently available knowledge of OIF. However, there may be other factors which are currently unknown or not specifically considered here.

3.1.1. Requirement 1: Nutrient supply from the lower overturning circulation cell

So-called "nutrient robbing" has been discussed as a biogeochemical side-effect reducing the efficiency of OIF (The Royal Society 2009). Nutrient robbing means that primary production stimulated by OIF enables biological drawdown of nutrients such as nitrate (N) and phosphate (P), which are no longer available to fuel primary production downstream of the OIF site (Sarmiento and Orr 1991; Gnanadesikan et al. 2003; Aumont and Bopp 2006; Oschlies et al. 2010; Hauck et al. 2018). As such, OIF can enhance biotic CO_2 sequestration at the location of fertilization but reduce sequestration at other locations where the nutrients would have been utilized otherwise.

In the Southern Ocean, the reduction of OIF-efficiency due to nutrient robbing can be minimized by restricting the application of OIF to locations south of the Southern Ocean Biogeochemical Divide (SOBD) (Sarmiento et al. 2010). The SOBD is the boundary between the upper and the lower overturning circulation cells in the surface ocean ((Marinov et al. 2006); Fig. 2A). North of the SOBD, nutrients upwelled within Upper Circumpolar Deep Water (UCDW) move net(northwards). The fraction of nutrients which are eventually subducted as Intermediate and Mode Waters as part of the upper overturning circulation cell ((Marshall and Speer 2012); Fig. 2A) without being utilized by primary producers are called preformed nutrients (Ito and Follows 2005). Intermediate and Mode waters remain relatively shallow (~1000 m) and are re-exposed to the surface decades to centuries after subduction so that the entrained pre-formed nutrients fuel primary production north of 30°S (Marinov et al. 2006; Palter et al. 2010; Primeau et al. 2013; Hauck et al. 2018). Thus, CO_2 sequestration through OIF north of the SOBD in the Southern Ocean would be reduced due to reductions in CO_2 sequestration outside the Southern Ocean at a later point in time (Gnanadesikan and Marinov 2008; Oschlies et al. 2010; Sarmiento et al. 2010; Primeau et al. 2013).

In contrast, nutrient robbing is reduced when OIF was operated south of the SOBD (Sarmiento et al. 2010). Here, nutrients upwelled within Lower Circumpolar Deep Water (LCDW) move (net)southward so that the fraction of nutrients that remains un-utilised by phytoplankton becomes entrained in Dense Shelf Water (DSW), the precursor of Antarctic Bottom Water (AABW) (Fig. 2A). These pre-formed nutrients are trapped in the deep ocean circulation cell and therefore are not utilized further downstream for photosynthetic primary production, simply because they are not exposed to sunlight outside the Southern Ocean. (Please note that this simplified scheme of an isolated lower overturning circulation cell neglects exchange of water and nutrients with the upper overturning cells, which has to the best of our knowledge not been quantified so far.)

The location of the SOBD has not been well constrained, possibly because the lower-resolution biogeochemical models used to derive and validate the conceptual framework of the SOBD (Marinov et al. 2006; Primeau et al. 2013) often have limited skill to correctly reproduce AABW formation pathways (Heuzé 2021). To narrow this knowledge gap, Xie et al. (2022) utilised a 1/10° physical model (ACCESS-OM2-01) to constrain the geographical location of the SOBD. In this accompanying study we found that the SOBD constitutes a circumpolar ring relatively close to Antarctica (Fig. 2B), shaped by several oceanographic features. Regions south of the SOBD consist mostly of the

continental shelves and extend slightly off the shelves in Eastern Antarctica (Fig. 2B). The results by Xie et al. (2022) suggest that OIF should be conducted in the blue areas mapped in Fig. 2B, since nutrient robbing and the associated reduction of CDR efficiency would be minimized. Importantly, their results also suggest that the SOBD is further south than all previous *in situ* OIF experiments in the Southern Ocean (Fig. 2B).

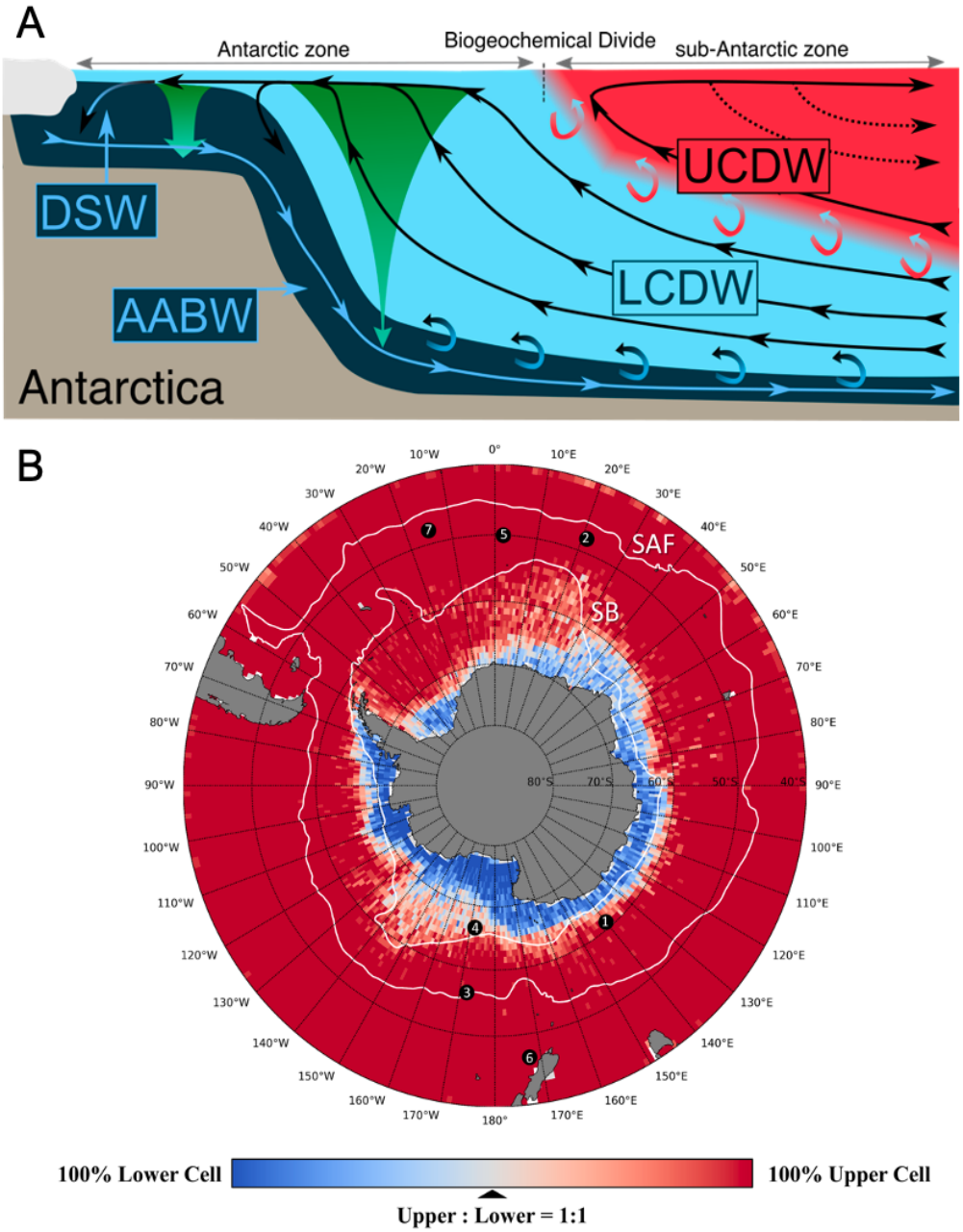

Figure 2. Physical conditions influencing the OIF potential in the Southern Ocean. (**A**) Schematic overview of zonal mean major water mass movements as indicated by black and blue arrows showing upwelling of Upper and Lower Circumpolar Deep Water (UCDW, LCDW), the origin of Dense Shelf Water (DSW), as well as sinking and

northward flow of Antarctic Bottom Water (AABW). The green downward arrows indicate carbon flux attenuation during sinking. Dashed arrows indicate the formations of Intermediate and Mode waters. The boundary separating the upper and lower overturning cells at the surface marks the Southern Ocean biogeochemical divide (Marinov et al. 2006). (**B**) Map showing the geographical location of the Southern Ocean biogeochemical divide assessed by virtual particle tracking in a 1/10 degree physical ocean model ACCESS-OM2-01 (Xie et al. 2022). Points indicate locations of previous meso-scale iron fertilization experiments: 1=SOIREE, 2=EisenEX, 3=SOFeX-N, 4=SOFeX-S, 5=EIFEX, 6=SAGE, 7=LOHAFEX (Yoon et al. 2018).

3.1.2. Requirement 2: Prevailing iron limitation

The first step in OIF is the stimulation of phytoplankton C-fixation by the fertilization of the surface ocean with iron. The fertilization can only have a stimulatory effect when iron is limiting C-fixation. Results synthesized here show that phytoplankton are not limited by iron when concentrations are >0.5 nM. Signs of iron-limitation (i.e. reduced growth) start to become apparent between >0.25 – 0.5 nM, while pronounced reduction of growth is widespread between 0 – 0.25 nM (Fig. 3A). Comparing these thresholds to in situ DFe concentrations suggests generally limiting DFe concentrations in Western Antarctica (Fig. 3B). Data coverage in Eastern Antarctica is sparse, although the few observations in the Davis Sea imply less limiting DFe conditions. Regions with sufficient temporal coverage such as the Ross Sea indicate iron-limited conditions from December to February (Fig. S4). The results of the analysis suggest that iron-limitation prevails in summer although natural DFe available early in the growth season may require the postponement of purposeful iron additions until the natural pool has been used up (Arrigo and Tagliabue 2005).

3.1.3. Requirement 3: Absence of phytoplankton light limitation

Low light availability is often considered another potential factor limiting or co-limiting phytoplankton growth in the Southern Ocean even during summer (Venables and Moore 2010). In cell cultures, light becomes limiting for several Southern Ocean phytoplankton species (on average) at 1.5 mol photons m^{-2} d^{-1} (Fig. 3C). This value is lower than the threshold for phytoplankton growth (3 mol photons m^{-2} d^{-1}) determined by Venables and Moore (2010) further north in the Southern Ocean. The mean mixed layer irradiance (I_{MLD}) during summer (December-February) was generally well above both of these thresholds, although there are noticeable gaps in the I_{MLD} coverage due to limited Argo observations near the shelves of Antarctica (Fig 3D). Accordingly, light should generally not limit phytoplankton growth during summer south of 60°S (Fig. 3D), which is in line with regional case studies including mesoscale experiments (Boyd et al. 2000). This trend suggests that OIF would stimulate primary production south of 60°S during summer when iron is (mildly) limiting phytoplankton growth.

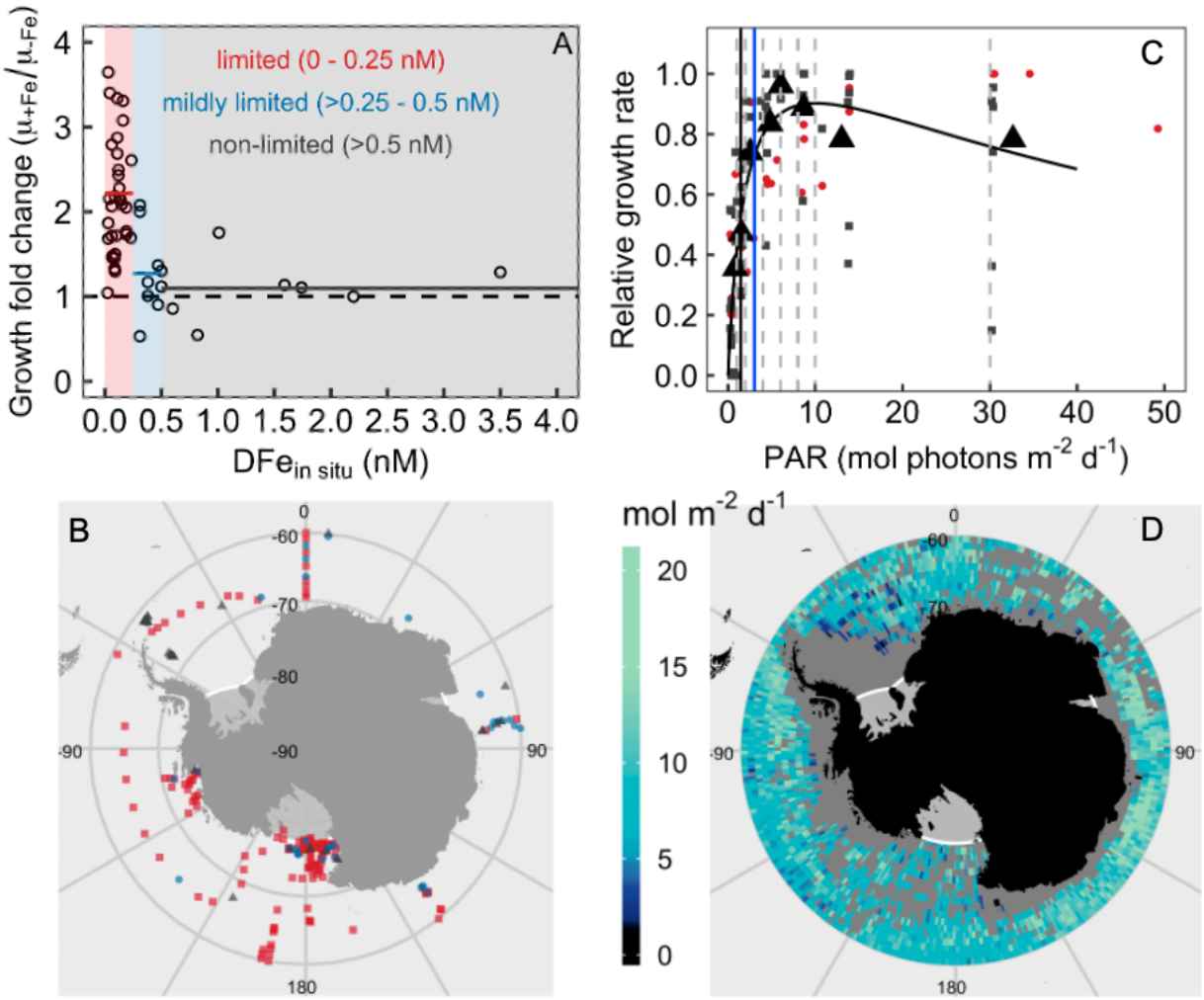

Figure 3. Phytoplankton iron and light limitation in the Southern Ocean. (**A**) The change of growth rates in DFe-enriched treatments relative to growth rates in the controls (μ_{+Fe}/μ_{-Fe}) is shown as a function of *in situ* DFe at the locations where the incubated water was collected. The horizontal lines are the μ_{+Fe}/μ_{-Fe} averages within the defined limitation ranges. (**B**) Map showing non-limiting (gray triangles), mildly-limiting (blue circles), and limiting (red squares) *in situ* DFe concentrations during summer (DJF). DFe data was from (Tagliabue et al. 2012). (**C**) Growth vs. irradiance curves from experiments with Southern Ocean diatoms (gray squares) and the haptophyte *Phaeocystis antarctica* (red circles). The larger black triangles show averages of all data within a bin (bins separated with vertical dashed lines). The black vertical line at 1.5 mol photons m^{-2} d^{-1} is the irradiance at which the onset of saturation occurs, calculated with the photosynthesis-irradiance model (black curve) by Eilers and Peeters (1988), while the blue vertical line indicates the 3 mol photons m^{-2} d^{-1} threshold for phytoplankton growth determined further north in the Southern Ocean from *in situ* data (Venables and Moore 2010). (**D**) Map showing that the mean mixed layer irradiance (I_{MLD}) is almost everywhere above 3 and even 1.5 mol photons m^{-2} d^{-1} during summer.

3.1.4. Requirement 4: Longer-term carbon storage

546 The second step in OIF, after the stimulation of C-fixation through fertilization, is the sequestration of
547 photosynthetically-fixed carbon into the deep ocean via various routes of the biological carbon pump (Gnanadesikan
548 and Marinov 2008; Boyd et al. 2019). In the context of OIF, it has often been assumed that the longevity of carbon
549 sequestration increases with the depth to which carbon is transported before it is respired (Lampitt et al. 2008;
550 Smetacek et al. 2012). However, this assumption does not take into account the 3-dimensional movement of water
551 masses through the Southern Ocean (Marshall and Speer 2012), which controls how long respired carbon remains in
552 the oceans' interior (England 1995; Siegel et al. 2021). For example, >80 % of OIF-derived carbon sinking to 1000 m
553 in the cyclonic Weddell Gyre could be re-exposed to the surface in <100 years because of deep-water upwelling
554 (Robinson et al. 2014), while longer-term storage (>>100 years) occurs when OIF-derived carbon is entrained in
555 forming dense waters at much shallower depths on the continental shelf that subsequently form AABW (Sarmiento et
556 al. 2010; Devries et al. 2012). There is currently no international legal or political framework that determines how
557 longevity is factored into the formulation of a carbon price, but it is likely that longer-term CO_2 sequestration leads to
558 considerably higher pricing (Ruseva et al. 2020). Hence, sequestration in upwelling CDW is less favorable than
559 sequestration in AABW, which is why we focus on the latter (but emphasizing that decadal-scale CO_2 storage still has
560 value). In the following sections we investigate two key mechanisms by which carbon could be transferred from the
561 surface to AABW, via both physical downwelling and gravitational sinking.
562 The simulation of physical downwelling of POC or DOC finds that POC and DOC are more likely to be exported
563 to depth via downwelling when OIF is conducted on, or close to, the continental shelf regions where dense water
564 formation occurs mostly during winter (Fig. S2). However, the probability for particle entrainment in overflowing
565 bottom waters within a year is generally <<25%. (Please note that one year was chosen as most organic carbon would
566 be respired within this timescale). We note that unresolved eddy diffusion not represented in the particle-tracking
567 experiment could possibly increase the entrainment of particles into AABW. This may expand the region with
568 substantial probabilities of entering AABW and therefore we consider our estimate to be conservative.
569 Gravitational sinking of organic particles is the main pathway that has been previously considered for OIF-derived
570 POC to be transferred from surface waters to depth (Boyd et al. 2000; Smetacek et al. 2012). In a Monte Carlo
571 approach, we generated 1000 plausible scenarios for the fraction of primary production reaching any given depth (Fig.
572 4A). This fraction converges towards a narrow range with increasing depth, mostly between 1-5% below 1000 m (Fig.
573 4B-E). The depth of the upper interface of the AABW is generally between 1000-4500 m off the Antarctic continental
574 shelf (Fig. 34F). Based on the median export-ratio (0.28) and b-value (0.96), we estimate the percentage of primary
575 production reaching AABW in offshore environments to range between 0.7-2.7%, except for some areas near the shelf
576 break (Fig. 4G). This range suggests: (i) a limited potential to transfer sinking OIF-derived POC from surface water
577 into AABW in offshore regions, and (ii) a ~4-fold range for sinking POC flux reaching AABW depending on where
578 within the offshore regions OIF is applied.
579 The potential for downward POC transfer to AABW via gravitational sinking is substantially higher on the
580 Antarctic continental shelves. Here, Dense Shelf Water (DSW), the denser precursor of AABW, is formed by surface
581 cooling and brine rejection during sea-ice formation (Williams et al. 2010; Ohshima et al. 2013). DSW overflows
582 across the shelf break following the seafloor topography but occupies relatively shallow depths that can extend to just

583 below the surface mixed layer (Morrison et al. 2020). This means that most, if not all, of the POC that escapes
584 remineralization in surface waters can potentially reach DSW in these continental shelf regions (Fig. 4H). The
585 problem, however, is that the sub-surface flow of DSW from formation regions to the shelf break is spatially localized
586 and occurs in highly episodic events on timescales of days. DSW tends to flow off the shelf along the western flanks
587 of undersea canyons in a limited number of locations along the continental shelf, with CDW transport onto the shelf
588 on the eastern flanks (Morrison et al. 2020). Accordingly, POC would be more likely to be sequestered when sinking
589 into subsurface water flowing along western flanks of the undersea canyons but potentially re-exposed to the
590 atmosphere when sinking on the eastern flanks. The exact location where POC sinks is challenging to predict because
591 it takes from days to several weeks following the iron fertilization until downward POC export commences (Boyd et
592 al. 2000; Buesseler et al. 2005; Smetacek et al. 2012). We estimated the regional potential for horizontal displacements
593 of POC for a one-month period using the virtual particle release experiment and found that neutrally buoyant POC
594 would generally travel <150 km total distance in one month in the Weddell and Ross Gyres and on the continental
595 shelves except for larger distances in coastal currents (Fig. S3). These horizontal displacements of POC, that occur
596 from the time of fertilization until the onset of POC export, must be anticipated for the site selection of the Fe-addition
597 to avoid POC export into a water mass that re-exposes respired POC (i.e., CO_2) to the atmosphere weeks to months
598 after the OIF operation. Hence, OIF on the shelves requires a profound understanding of deep-water formation
599 mechanisms and pathways.
600 The calculation of gravitational POC transfer efficiency from surface into AABW is based on mean export-
601 ratios and b-values published for the Southern Ocean (Tables S4 and S5), with large variability based on the wide
602 range of observations (Fig 4). Consistent with observations, mesoscale OIF experiments in the Southern Ocean have
603 found variable responses of downward POC export to fertilization. Some observations suggest comparable export to
604 naturally-occurring blooms (Buesseler et al. 2005), while another study reports extremely efficient export (Smetacek
605 et al. 2012). Two studies found no noticeable increase in export, although this was arguably because observations
606 stopped before the export commenced (Boyd et al. 2000; Smetacek et al. 2012). POC transfer efficiency has frequently
607 been shown to be controlled by pelagic community structure (Boyd and Newton 1995; Wassmann 1998; Guidi et al.
608 2009; Assmy et al. 2013). Hence, it could be argued that targeting 'transfer-efficient' communities for OIF, or even
609 seeding them alongside OIF operations, could optimize e-ratios and b-values and lead to more POC sequestration than
610 Fig. 4 suggests. For example, fertilizing phytoplankton communities with abundant *Phaeocystis antarctica* may
611 increase carbon sequestration compared to fertilized diatom communities due to *Phaeocystis*' inherently higher
612 Carbon to nutrient ratio (Arrigo et al. 1999). However, our ability to predict POC transfer efficiency based on plankton
613 community composition is poor (Burd et al. 2016), suggesting that such optimization is unlikely to be successful with
614 our current level of understanding (and the seeding of phytoplankton communities seems unlikely to receive social
615 license and/or legal allowance). Furthermore, phytoplankton communities that result in high transfer-efficiencies may
616 not prevail in a target region during the short period in summer where conditions enable OIF (Arrigo and Tagliabue
617 2005). In light of these limitations, it seems justifiable to base our estimates of POC transfer to AABW on the wide
618 range of observations and thus to accept that the CDR efficiency of OIF is currently rather unpredictable within the
619 estimated bounds.

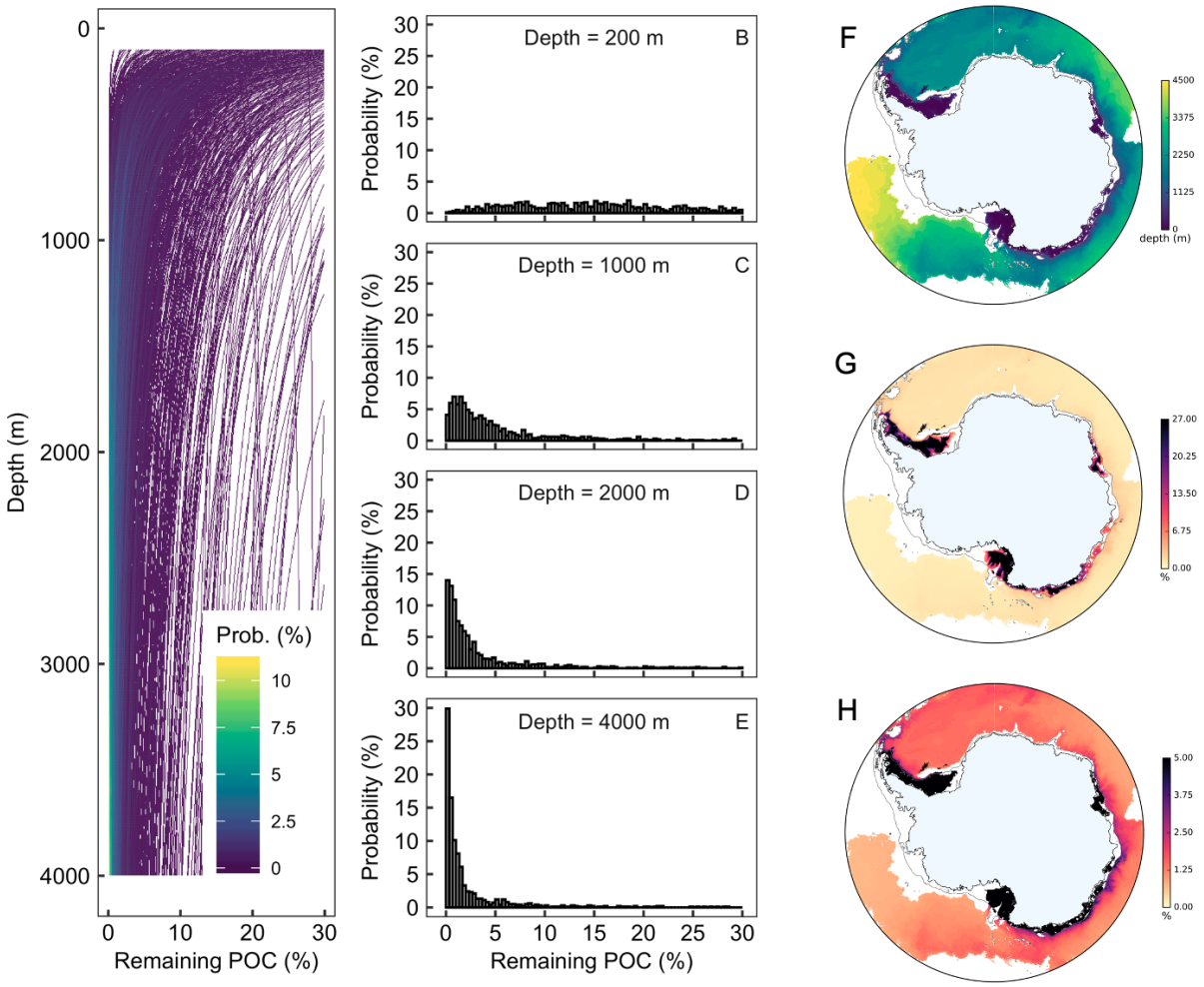

Figure 4. Gravitational OIF-mediated POC export. (**A**) Fraction of primary production reaching depth. Shown are 1000 profiles based on the Monte Carlo approach (see text for details). The density color code indicates with what probability the profiles occur in the space of the plot. (**B-E**) Probabilities of remaining primary production at distinct depth horizons based on the 1000 profiles. (**F**) Depth of the upper interface of the AABW layer. (**G**) Remaining primary production at the depth of the AABW layer, calculated with the median export-ratio (0.28) and median b-value (0.96). (**H**) Same as in (**G**) but with a narrower scaling to better illustrate differences in the offshore locations.

3.1.5. Requirement 5: air-sea CO_2 equilibration

The third step in OIF, after C-fixation and carbon export to deep waters, is the transfer of atmospheric CO_2 into the ocean (Gnanadesikan and Marinov 2008). We employed a "bucket" approach to estimate what fraction of a water parcel with a seawater CO_2 deficit (induced by OIF) would be replenished with atmospheric CO_2 before the water parcel was subducted (i.e. f_{Eq} as defined in section 2.4). The approach has some strengths and weaknesses which need to be highlighted before discussing the outcome of the calculations. Strengths are: 1) comparing the OIF with the no-

OIF scenario accounts for "expected" background changes in DIC from ocean processes including vertical transport, eddy mixing and storm mixing that are reflected in observations. This leads to a more realistic representation of air-sea CO_2 exchange, since natural variability is considered in the calculation. 2) Using lagrangian particles to trace water parcels enables us to link f_{Eq} with the origin of the OIF patch. This provides a gridded dataset which is crucial for the spatially resolved OIF (cost-)efficiency analysis, the key novelty of the study (sections 3.3 and 3.4). 3) Lagrangian particle tracking is computationally relatively inexpensive, enabling the use of high-resolution model output. This is critical for improved representation of deep-water formation (Heuzé 2021). Weaknesses are: 1) The approach neglects patch dilution, which reduces air-sea pCO_2 gradients in the fertilized patch but increases the surface area for CO_2 exchange with the atmosphere. These are opposing effects on air-sea CO_2 exchange and we are unable to quantify their relative influence. 2) Patch dilution can also increase productivity (Lehahn et al. 2017) so that an initial DIC deficit of 35 µmol/kg may increase over time. This is not accounted for in our calculations. 3) The assumption that influx is terminated upon subduction of a water parcel (Fig. 1) is simplistic since a parcel could resurface after its subduction and CO_2 influx could continue. Despite the weaknesses, our approach seems to provide a useful overview where in the Southern Ocean limitations on OIF set by air-sea CO_2 exchange could become problematic. As described in the next paragraph, air-sea CO_2 exchange was estimated to only limit OIF (cost-)efficiency in a few AABW formation regions on the shelves. This is qualitatively similar to previous findings (Arrigo and Tagliabue 2005; Gnanadesikan and Marinov 2008) and provides some confidence that our estimates are reasonable.

The calculations suggest that af_{Eq} is generally >50% off the continental shelves (Fig. 5A). Fig. 5B shows that this degree of re-equilibration with atmospheric CO_2 is several-fold more than needed to equilibrate the amount of CO_2 sequestered in AABW off the shelves (i.e. $f_{Seq} \geq 1$, or ≥100% as shown in Fig. 5B). Accordingly, air-sea CO_2 influx is unlikely to constrain the efficiency of OIF in the open Southern Ocean, at least in areas where the limited extent of sea ice allows this type of analytical approach.

In contrast, air-sea CO_2 influx can limit OIF efficiency in some parts of the Antarctic shelf, most noticeably in the Ross Sea where $f_{Seq} < 1$ near the coast (Fig. 5B). This result is broadly consistent with a regional model that also identified air-sea CO_2 influx as a potential limitation of OIF in the area (Arrigo and Tagliabue 2005). On other shelf areas there are only some scattered locations around Eastern Antarctica and at the tip of the Antarctic Peninsula where air-sea CO_2 influx is not sufficient to match the amount of POC sequestered in AABW (Fig. 4B). The reason for the insufficiency in these regions are twofold. First, the identified shelf regions are relatively efficient in transferring POC from the surface to AABW because AABW (or DSW as its precursor) can be present at shallow depths (Fig. 4F). Thus, relatively high amounts of POC are sequestered in AABW (Fig. 4G) so that more atmospheric CO_2 influx is needed to match the amount of sequestered POC. Second, AABW can form in the identified regions shortly after the simulated OIF operation in January so that water parcels have short residence times in the surface thereby restricting the time for air-sea CO_2 influx.

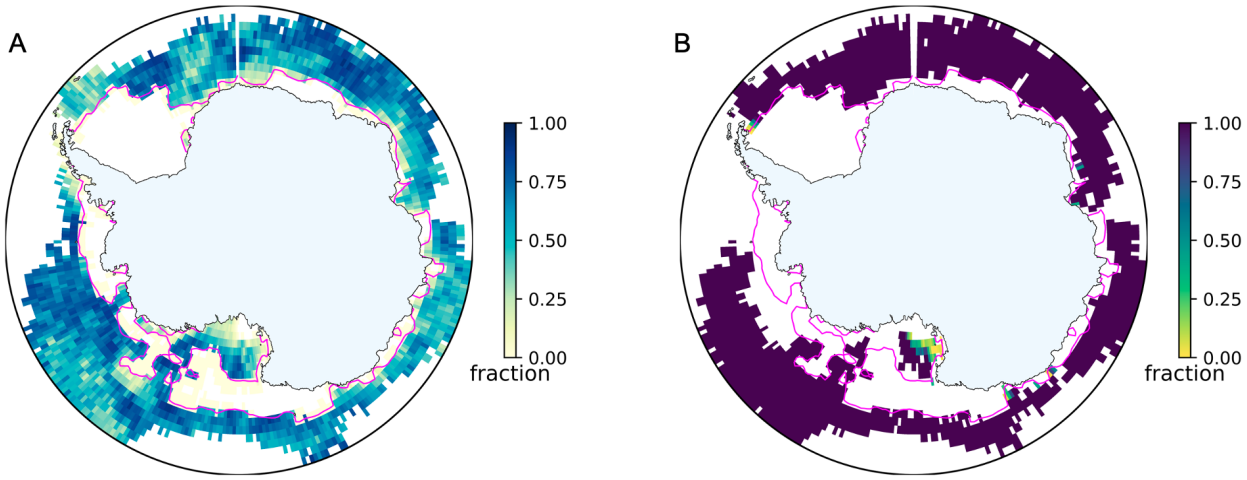

Figure 5. Timescales of air-sea CO_2 exchange estimates. (**A**) Fraction of CO_2 equilibration (f_{Eq}) for an initial 35 µmol kg^{-1} CO_2 deficit before virtual particles (as equivalents of water masses) leave the surface mixed layer (and therefore contact with the atmosphere). (**B**) f_{Seq}, which indicates if there is sufficient air-sea CO_2 exchange to match the amount of POC sequestered in AABW. The magenta contours in A and B show the 60% sea ice concentration at the time of particle release (Jan 3). Sea ice concentrations >60% impeded our analysis so that these regions could not be assessed.

3.2. Constraints to the maximum potential of Southern Ocean Iron Fertilisation

In Section 3.1.1. we argued to fuel OIF with macronutrients from the lower overturning circulation cell. This requirement also constrains the theoretical maximum potential for CDR with OIF in the Southern Ocean. The supply of surface water into the lower cell is estimated as 5.4 +/-1.7 Sv (Orsi et al. 2002), which contains ~1.5 µM of preformed P (Ito and Follows 2005; Duteil et al. 2012). Assuming a C/P ratio of 111 +/-7 for Antarctic phytoplankton blooms (Arrigo et al. 1999) and 100% utilization of preformed P in the surface via OIF provides an upper bound of 1.3 ±1.2 Gt CO_2 $year^{-1}$.

Undoubtedly, these assumptions mean that our estimate of the maximum CDR potential has several conspicuous limitations. First, the depletion of macronutrients due to OIF at the surface of the Southern Ocean would increase the vertical macronutrient gradient thereby increasing the eddy diffusive flux into the surface layer from below for the time period that surface nutrient concentrations remain depleted. This altered gradient could potentially increase the supply of N and P into the surface layer that could be utilized by OIF and thus enhance the theoretical maximum. However, the depletion of the inventory of preformed nutrients may not be attainable even if phytoplankton growth is not limited by iron, because the residence time of preformed nutrients in the euphotic zone may be too short for depletion. These residence times are to the best of our knowledge unknown. Thus, it is not possible to determine if nutrients are present for sufficiently long in the sunlit euphotic zone (thereby enabling their photosynthetic utilization) to facilitate complete drawdown.

It is also worth noting that a 100% utilization of 1.5 µM preformed P in the surface would cause a build up of ~167 µM POC (C/P of 111 mol/mol; (Arrigo et al. 1999)), which would consume ~240 µM of dissolved oxygen if all POC was remineralised in AABW (C/O_2 of 117/170 mol/mol; (Sarmiento and Gruber 2006)). This is most, if not all oxygen ventilated to the deep ocean within forming AABW (Sarmiento and Gruber 2006; Katsumata et al. 2015), and would therefore cause severe de-oxygenation. Accordingly, OIF near Antarctica would need to be limited to a yet to be determined "sustainable maximum", which is likely well below the theoretical maximum estimated above.

To avoid confusion, we note that our subsequent results and discussion will not further address criteria determining the "theoretical", "attainable" or "sustainable" maximum CDR potential of OIF. Instead, our focus is on criteria that can limit the CDR potential per unit area and thus instead we investigate the (cost-)efficiency of OIF, which is different from previous expert-assessments or syntheses where there was often a focus on the maximum CDR potential of OIF (Strong et al. 2009; Williamson et al. 2012; Gattuso et al. 2018). Our argument for focusing on (cost-)efficiency is that this parameter may be more important from a stakeholder's economic perspective (which may be countries or private enterprises) and may therefore be more decisive for a potential real-world implementation of OIF (Rickels et al. 2012; Bellamy and Geden 2019).

3.3. Spatial patterns of CDR (cost-)efficiency

The spatial analysis of CDR (t CO_2 km^{-2}) and associated costs (US\$ t^{-1} CO_2^{-1}) reveals pronounced regional differences in both parameters (Fig. 6). Most favorable conditions are found on or very close to Antarctic shelves where AABW or its precursors are relatively shallow (Fig. 2A and Fig. 3F). In the Ross Sea, for example, >2 t CO_2 km^{-2} can be sequestered at a cost much below 100 US\$ t^{-1} CO_2^{-1}. However, limited air-sea CO_2 influx can still reduce CDR and increase the costs in the Ross Sea near the coast (Fig. 6). Similarly (cost-)efficient conditions can be found at the tip of the Antarctic Peninsula, Prydz Bay, and a few smaller spots at the coast of Eastern Antarctica (Fig. 6). In contrast, CDR declines and costs rise sharply further offshore in the open Southern Ocean. Here, CDR are largely below 0 t CO_2 km^{-2} (gray areas in Fig. 56A) and costs are negative (black areas in Fig. 6B) because the emissions associated with iron delivery and N_2O-related offsets are higher than CDR.

There are several limitations in the spatial analysis of CDR (cost-)efficiency. First, relatively large data gaps are present throughout the study region due to the influence of sea-ice on the analysis of air-sea CO_2 transfer (Fig 5). Thus, particularly (cost-)efficient or inefficient regions may have been missed. Second, one requirement for our analysis is that OIF would be restricted to south of the SOBD to limit offsets in (cost-)efficiency due to nutrient robbing (section 3.1.1.). However, our spatial analysis partially extends to regions north of the SOBD (compare Figs. 2B and 6). Here, CDR efficiency would further decline (costs would increase) when accounting for the reduction of downstream productivity due to nutrient robbing. We have not factored this offset into eq. 15 because the complicated global ocean teleconnections between nutrient drawdown in the Southern Ocean and nutrient availability outside the Southern Ocean make it difficult to constrain (Hauck et al. 2018). Third, our cost-calculation does not account for purchasing or chartering a ship but considers a "ship of opportunity scenario" that has multiple tasks and can carry out OIF opportunistically during the S. Ocean productivity season. Likewise, costs to gain legal permission for OIF

or to measure, report, or verify CDR were also not considered in the calculations as we are unable to constrain them. Assuming these factors would double the operational costs (eq. 20), it would double the costs per tonne CO_2 at any given location in Fig. 6B. Fourth, we defined that POC sequestration in upwelling Southern Ocean water masses like CDW would have no value because these re-expose respired CO_2 to the surface within decades (Robinson et al. 2014; Tamsitt et al. 2017; Siegel et al. 2021). Instead, we defined that POC sequestration in AABW has maximum value as it locks POC in the deep-ocean for much longer timescales (Siegel et al. 2021). This categorization was necessary because we were unable to link a sequestration timescale to every depth and location where OIF-derived organic carbon is potentially respired. In reality, however, longer-term POC storage is certainly more valuable than short-term storage but short-term storage is not worthless (Ruseva et al., 2020). Concepts to rate the amount of sequestered carbon with its sequestration longevity (e.g. "ton-year accounting"; (Chay et al. 2022)) may make short-term CDR more valuable off the shelves than the maps shown in Fig. 6 suggest. Thus, it needs to be kept in mind that our analysis of (cost-)efficiency leads to results that are valid under the assumptions made here but could be modified when more sophisticated carbon accounting methodology is applied.

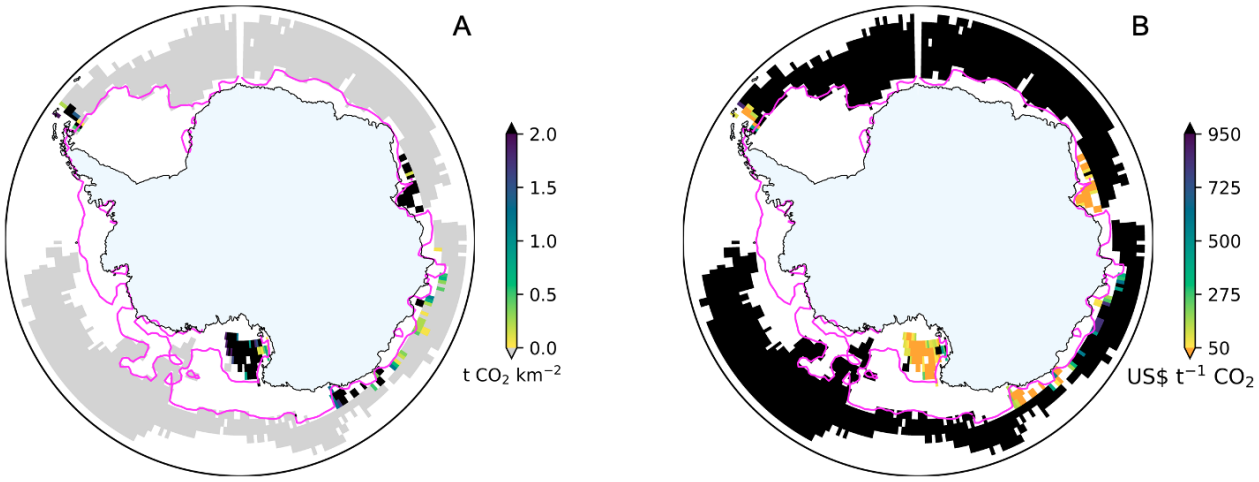

Figure 6. Magnitude of CDR and associated costs. (**A**) CDR achieved south of 60°S as calculated with equation 15, using median e-ratio and b-value to calculate flux attenuation. (**B**) Costs per t CO_2 sequestered. Values were calculated by dividing an intermediate $costs_{area}$ estimate for OIF (74 \$US km^{-2}, Table S6) by CDR from (**A**) as in eq. (20).

3.4. Variability in OIF (cost-)efficiency

We used a Monte Carlo approach to estimate the likelihood distributions for longer-term CDR (defined above as POC transfer into AABW) for two different AABW depths (200 and 1000 m) and for complete or incomplete CO_2 equilibration (f_{Seq} = 0.5 or 1). These two conditions encompass the most relevant parameter range for an on-the-shelf (200 m, 0.5) and off-the-shelf (1000 m, 1) scenario (Fig. 7).

Simulated variability in either f_{N2O} or $O_{transport}$ had a small influence on CDR variability in all of the scenarios (Fig. 7A, B). Simulated variability in C/Fe had a larger influence on CDR variability but only for the 200 m scenario (Fig.

7A, B). Simulated variability in POC_{AABW} had by far the largest influence on CDR variability in all scenarios considered here (hence constraining the factors that control export flux attenuation offers the greatest potential for improving the predictability of CDR as has been discussed in section 3.1.4.). Unsurprisingly, CDR variability is highest when simulating variability in all four components (f_{N2O}, $O_{transport}$, C/Fe and POC_{AABW}) simultaneously. The variability in costs is shown as histograms in Fig. 7C and D. Here, turquoise and red histograms show cost distributions for an AABW surface depth of 200 and 1000 m respectively. Simulations shown in Fig. 7C assume that f_{Seq}=1, i.e. that all CO_2 sequestered from seawater is matched with the influx of atmospheric CO_2. In this case, there is a 98% probability that costs will be between 0-100 US$ t^{-1} CO_2^{-1} when AABW is only 200 m deep. However, the probability of being in this price range is only 27% when AABW is at 1000 m, and there is a 58% chance that the costs are negative, meaning that OIF generated more CO_2 equivalents through shipping emissions and N_2O generation than it sequestered (Fig. 7C). Cost distributions become less favorable under the assumption that only half of the CO_2 sequestered from seawater is matched by atmospheric CO_2 influx (i.e. f_{Seq}=0.5; Fig. 7D), a scenario that can occur in some shelf regions (Fig. 5B). Here, costs are only between 0-100 US$ t^{-1} CO_2^{-1} in 86% (AABW at 200 m) and 12% (AABW at 1000 m) of the cases. Negative costs still hardly occur for the 200 m AABW scenario (0.6% of cases) but predominate for the 1000 m AABW scenario (80% of cases).

An important takeaway from the assessment of variability is that CDR is negative in the majority of cases when AABW is deeper than 1000 m. Thus, although there still is a chance that CDR is (cost-)efficient under circumstances where mainly flux attenuation is low (section 3.1.4.), the likelihood for this is low. Accordingly, there is a high risk for failed OIF over large parts of the open Southern Ocean where AABW is deeper than 1000 m (Fig. 4F). The variability of OIF (cost-)efficiency is also considerable when AABW occurs at 200 m depth (possible in some shelf regions, Fig. 4F). However, costs are in most cases between only 0-100 US$ t^{-1} CO_2^{-1}. Any costs within this range are low compared to other CDR methods (Fuss et al. 2018) and therefore potentially attractive from an economic standpoint. Nevertheless, the unpredictability of costs, even within this low range, remains a challenge since carbon markets may demand more predictable CDR and costs.

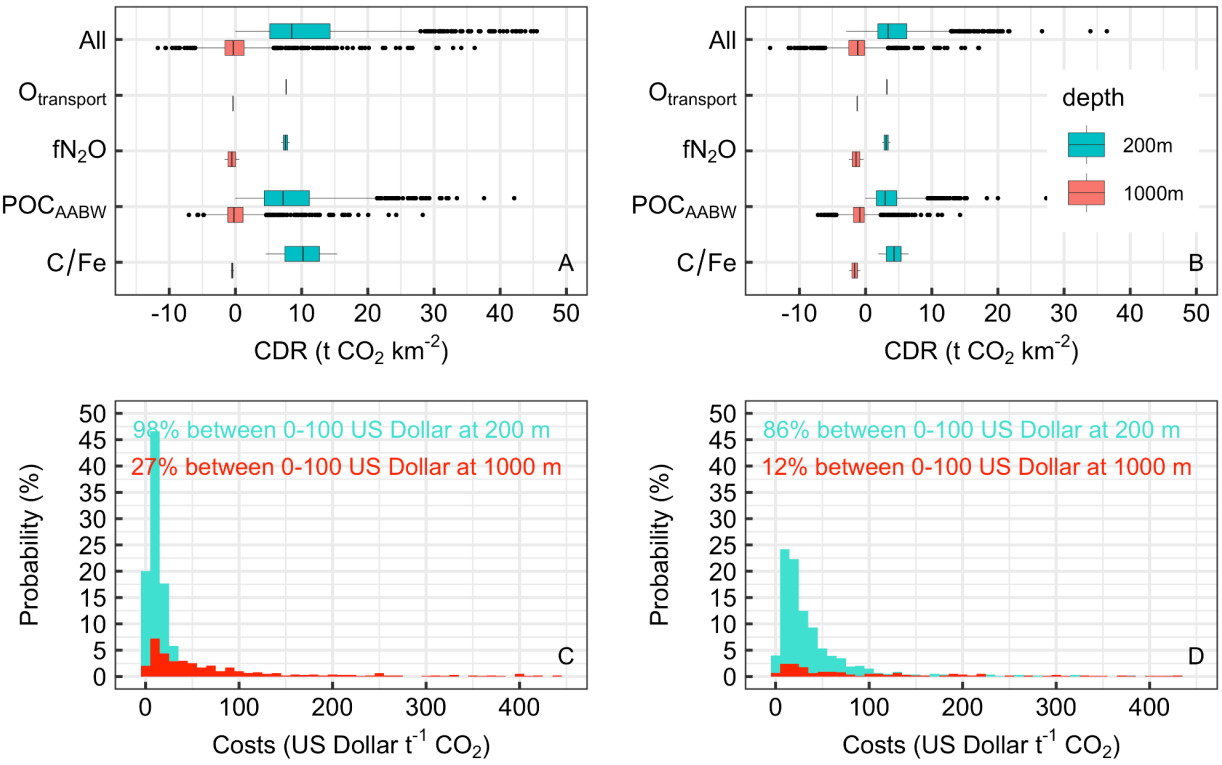

Figure 7. Variability in the (cost-)efficiency of OIF. (**A**) Results from the Monte Carlo simulations (N=1000) where individual components of eq. 15 were varied within their data-constrained ranges to assess their influence on CDR variability. Boxplots show the median, 25 and 75% percentiles (boxes), minimum/maximum (whiskers), and outliers (dots). Turquoise and red boxes are scenarios where the AABW surface layer is at 200 and 1000 m, respectively. f_{Seq} was set to 1 in these calculations, meaning that air-sea CO_2 influx puts no constraints on the CDR. (**B**) Same as in (**A**) but assuming f_{Seq}=0.5. (**C**) Histogram of OIF costs in scenarios where the AABW surface layer is at 200 m (red) or 1000 m (turquoise), respectively and f_{Seq} = 1. (**D**) Same as in (**C**) but with f_{Seq} = 0.5.

3.5. Environmental and legal ramifications

For OIF to move forward, CDR benefits (as well as environmental side-effects not considered in this study) would need to be re-evaluated within at least 4 partially overlapping layers of international and domestic law (Fig. 8). The 1991 Madrid Protocol to the Antarctic Treaty (covering the area south of 60°S) commits to 'comprehensive protection of the Antarctic environment and dependent and associated ecosystems'. The Ross Sea, which we identify as a cost-efficient region for OIF (Fig. 6), is the location of a marine protected area formed under the Commission for the Conservation of Antarctic Marine Living Resources (CCAMLR), so it may be very difficult for OIF to proceed there. More concrete rules apply to member states of the 1972 UN London Convention on Marine Pollution (currently 87) and its 1996 London Protocol (currently 53). Both of these treaties regulate ocean dumping of waste in the ocean. If OIF activities are only for 'legitimate scientific research' they are not considered 'dumping'. However, once OIF activities upscale beyond legitimate scientific research, the position under the two treaties diverges. The London

Convention would likely allow its member states to issue a permit for OIF, while OIF would likely be prohibited for member states in the London Protocol. The environmental and legal ramifications underscore the wide-ranging challenges of OIF, which go far beyond solving open questions in physical, chemical, and biological oceanography (Rohr 2019).

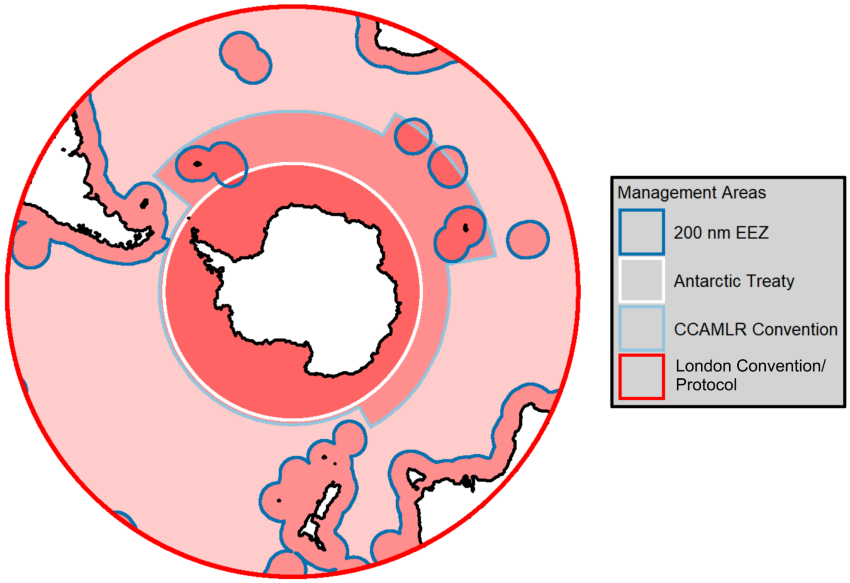

Figure 8. Legal constraints on OIF in the Southern Ocean. The map shows 4 layers of international or domestic law around Antarctica and Sub-Antarctic islands. Each layer is shaded in red with overlapping law leading to a more reddish color. The London Convention (LC) and London Protocol (LP) apply globally. National law applies within the exclusive economic zones of states, including the sub-Antarctic islands. CCAMLR governs marine living resources in sectors around Antarctica. The Antarctic Treaty applies south of 60°S.

4. Conclusions

The analysis presented here considers different biogeochemical variables which affect the CDR efficiency of OIF. These variables were assessed consecutively and finally synthesized into spatially resolved costs per tonne CO_2 removed. The focus on (cost-)efficiency was motivated by the notion that the implementation of different CDR methods is more likely driven by their (cost-)efficiency than their maximum CDR capacity in the Earth system (Rickels et al. 2012; Bellamy and Geden 2019). The approach chosen here to evaluate spatially resolved (cost-)efficiency in the Southern Ocean has several limitations and required assumptions on how future carbon accounting may function. For example, there may be other biogeochemical factors not considered here (e.g. DOC) that could modify (cost-)efficiency. However, the framework allows for updating and can thus be adapted and improved over time.

The analysis of variability in (cost-)efficiency underlines that one key challenge for OIF remains the predictability of CDR, consistent with conclusions made from the first era of OIF in situ experiments during the 1990s and early 2000s (de Baar et al. 2005; Boyd et al. 2007; Yoon et al. 2018). OIF will only become a credible method if the amounts of CDR can be accounted for accurately and with a precision that satisfies widely agreed accounting criteria which have yet to be developed (Arcusa and Sprenkle-Hyppolite 2022). It is questionable that the level of variability assessed here, spanning several orders of magnitude (Fig. 6), will satisfy future accounting standards. Thus, progressing OIF requires drastically improved understanding of the factors modulating CDR (i.e., primarily flux attenuation, see section 3.1.4) or requires the ability to precisely determine these factors empirically for individual OIF deployments. Our analysis is timely as there is renewed interest in OIF for large-scale CDR operations. A recent report on marine CDR methods called for 290 million US$ to assess OIF research priorities within 10 years (NASEM 2021) and there are ongoing efforts to establish new field research (Buesseler et al. 2023). Guidance for these emerging research efforts is already available in many papers, which identified maximum potentials of OIF, side-effects, and where in the oceans OIF may lead to the highest CDR (e.g. Aumont and Bopp 2006; Oschlies et al. 2010; Sarmiento et al. 2010). Our study utilizes conceptual understanding from these studies to derive, to the best of our knowledge, the first circumpolar and spatially resolved analysis of OIF (cost-)efficiency south of 60°S. The key novelty is that OIF efficiency is very low and costs are very high in most parts of the open Southern Ocean, such that OIF only seems to be feasible on some parts of the Antarctic shelf. This outcome could steer emerging research efforts towards these rather small areas of the Southern Ocean where OIF costs can be below 100 US$ t^{-1} CO_2^{-1}. However, this spatial restriction also means that the maximum potential of OIF is limited (we estimated 1.3 ±1.2 Gt CO_2 $year^{-1}$ under very optimistic, likely unrealistic, assumptions).

Overall, our analysis provides little incentive to further explore OIF in the open Southern Ocean south of 60°S. (Cost-)efficient OIF in these regions would require that OIF predictably generates very efficient POC transfer to great depth, as has been observed only in one study so far (Smetacek et al. 2012). (But note that even efficient POC transfer would not solve the problem of "nutrient robbing" discussed in section 3.1.1). While we find such highly (cost-)efficient cases for open ocean regions also within the variability determined here, they are the exception rather than the rule (Fig. 7). In contrast, our analysis suggests that there is value to further explore the concept of OIF on some Antarctic shelves. However, even if future research confirmed a high (cost-)efficiency, up-scaling beyond scientific research seems unlikely in the near future due to international treaties (section 3.5) and public perceptions (Cox et al. 2021). Thus, the benefit of shelf OIF, with its limited maximum CDR potential, would have to be carefully evaluated against its environmental implications.

Acknowledgements

The authors thank Argo, the NOAA National Sea Ice Data Center, the National Centers for Environmental Information and Remote Sensing Systems, and NASA Giovanni for openly providing the climatological data used in this study. We also thank Alessandro Tagliabue for kindly providing dissolved iron data. Argo data were collected and made freely available by the International Argo Program and the national programs that contribute to it (http://www.argo.ucsd.edu; http://argo.jcommops.org; http://doi.org/10.17882/42182). The Argo Program is part of the Global Ocean Observing System. NASA Giovanni is developed and maintained by the NASA GES DISC. We

acknowledge the mission scientists and Principal Investigators who provided data. We also thank two excellent reviewers and the editor for thoughtful and constructive comments.

Funding
Future Fellowship by the Australian Research Council FT200100846 (LTB)
CSHOR, a joint research Centre for Southern Hemisphere Ocean Research between QNLM and CSIRO (VT).
Laureate Fellowship by the Australian Research Council FL160100131 (PWB)
Australian Antarctic Program Partnership ASCI000002 (RFS)

Author contributions
Conceptualization: LTB, PWB
Methodology: LTB, VT, KB
Analyses: LTB, VT, KB, EL-C, JM, YX
Visualization: LTB, VT, KB, YX
Writing-original draft: LTB, VT, KB
Writing-review & editing: LTB, PWB, VT, KB, RFS, JM, EL-C

Competing interests
The authors declare no competing interests.

Data and materials availability
All data compiled from the literature is made available in the supplement. Data downloaded for calculations is referenced in the methods section. The Lagrangian particle trajectory output used in this analysis and the derived data can be found on https://zenodo.org/ under DOI: 10.5281/zenodo.5576833.

References

Arcusa, S., and S. Sprenkle-Hyppolite. 2022. Snapshot of the Carbon Dioxide Removal certification and standards ecosystem (2021–2022). Clim. Policy 1–14. doi:10.1080/14693062.2022.2094308

Arrigo, K. R., D. H. Robinson, D. L. Worthen, R. B. Dunbar, G. R. DiTullio, M. VanWoert, and M. P. Lizotte. 1999. Phytoplankton Community Structure and the Drawdown of Nutrients and CO2 in the Southern Ocean. Science (80-.). **283**: 365–367. doi:10.1126/science.283.5400.365

Arrigo, K. R., and A. Tagliabue. 2005. Iron in the Ross Sea: 2. Impact of discrete iron addition strategies. J. Geophys. Res. C Ocean. **110**: 1–16. doi:10.1029/2004JC002568

Assmy, P., V. Smetacek, M. Montresor, and others. 2013. Thick-shelled, grazer-protected diatoms decouple ocean carbon and silicon cycles in the iron-limited Antarctic Circumpolar Current. Proc. Natl. Acad. Sci. **110**: 20633–20638. doi:10.1073/pnas.1309345110

Aumont, O., and L. Bopp. 2006. Globalizing results from ocean in situ iron fertilization studies. Global Biogeochem. Cycles **20**: 1–15. doi:10.1029/2005GB002591

de Baar, H. J. W., P. W. Boyd, K. H. Coale, and others. 2005. Synthesis of iron fertilization experiments: From the iron age in the age of enlightenment. J. Geophys. Res. C Ocean. **110**: 1–24. doi:10.1029/2004JC002601

Bellamy, R., and O. Geden. 2019. Govern CO2 removal from the ground up. Nat. Geosci. **12**: 874–876. doi:10.1038/s41561-019-0475-7

Bowie, A. R., M. T. Maldonado, R. D. Frew, and others. 2001. The fate of added iron during a mesoscale fertilisation experiment in the Southern Ocean. Deep. Res. Part II Top. Stud. Oceanogr. **48**: 2703–2743. doi:10.1016/S0967-0645(01)00015-7

Boyd, P., and P. Newton. 1995. Evidence of the potential influence of planktonic community structure on the interannual variability of particulate organic carbon flux. Deep Sea Res. Part I Oceanogr. Res. Pap. **42**: 619–639.

Boyd, P. W., H. Claustre, M. Levy, D. A. Siegel, and T. Weber. 2019. Multi-faceted particle pumps drive carbon sequestration in the ocean. Nature **568**: 327–335. doi:10.1038/s41586-019-1098-2

Boyd, P. W., T. Jickells, C. S. Law, and others. 2007. Mesoscale Iron Enrichment Experiments 1993-2005: Synthesis and Future Directions. Science (80-.). **315**: 612–617. doi:10.1126/science.1131669

Boyd, P. W., C. S. Law, C. S. Wong, and others. 2004. The decline and fate of an iron-induced subarctic

phytoplankton bloom. Nature **428**: 549–553. doi:10.1038/nature02437
Boyd, P. W., A. J. Watson, C. S. Law, and others. 2000. A mesoscale phytoplankton bloom in the polar Southern Ocean stimulated by iron fertilization. Nature **407**: 695–702. doi:10.1038/35037500
Buesseler, K., F. Chai, D. Karl, and others. 2023. Ocean iron fertilization: assessing its potential as a climate solution.
Buesseler, K. O. 2012. T he great iron dump. Nature **487**: 305–306. doi:10.1038/487305a
Buesseler, K. O., J. E. Andrews, S. M. Pike, M. A. Charette, L. E. Goldson, M. A. Brzezinski, and V. P. Lance. 2005. Particle export during the Southern Ocean Iron Experiment (SOFeX). Limnol. Oceanogr. **50**: 311–327. doi:10.4319/lo.2005.50.1.0311
Burd, A. B., A. Buchan, M. Church, M. Landry, A. McDonnell, U. Passow, D. Steinberg, and H. Benway. 2016. Towards a transformative understanding of the ocean s biological pump: Priorities for future research.
Butterworth, B. J., and S. D. Miller. 2016. Air-sea exchange of carbon dioxide in the Southern Ocean and Antarctic marginal ice zone. Geophys. Res. Lett. **43**: 7223–7230. doi:10.1002/2016GL069581
Campbell, J. W., and T. Aarup. 1989. Photosynthetically available radiation at high latitudes. Limnol. Oceanogr. **34**: 1490–1499. doi:10.4319/lo.1989.34.8.1490
Carter, B. R., R. A. Feely, N. L. Williams, A. G. Dickson, M. B. Fong, and Y. Takeshita. 2018. Updated methods for global locally interpolated estimation of alkalinity, pH, and nitrate. Limnol. Oceanogr. Methods **16**: 119–131. doi:10.1002/lom3.10232
Chay, F., G. Badgley, K. Martin, J. Freeman, J. Hamman, and D. Cullenward. 2022. Unpacking ton-year accounting.
Cox, E., M. Boettcher, E. Spence, and R. Bellamy. 2021. Casting a Wider Net on Ocean NETs. Front. Clim. **3**. doi:10.3389/fclim.2021.576294
Devries, T., F. Primeau, and C. Deutsch. 2012. The sequestration efficiency of the biological pump. Geophys. Res. Lett. **39**: 1–5. doi:10.1029/2012GL051963
Duteil, O., W. Koeve, A. Oschlies, and others. 2012. Preformed and regenerated phosphate in ocean general circulation models- can right total concentrations be wrong? Biogeosciences **9**: 1797–1807. doi:10.5194/bg-9-1797-2012
Eilers, P. H. C., and J. C. H. Peeters. 1988. A model for the relationship between light intensity and the rate of photosynthesis in phytoplankton. Ecol. Modell. **42**: 199–215. doi:10.1016/0304-3800(88)90057-9
England, M. H. 1995. The age of water and ventilation timescales in a global ocean model. J. Phys. Oceanogr. **25**: 2756–2777. doi:10.1175/1520-0485(1995)025<2756:TAOWAV>2.0.CO;2
Fu, W., and W. L. Wang. 2022. Biogeochemical Equilibrium Responses to Maximal Productivity in High Nutrient Low Chlorophyll Regions. J. Geophys. Res. Biogeosciences **127**: 1–13. doi:10.1029/2021JG006636
Fuss, S., W. F. Lamb, M. W. Callaghan, and others. 2018. Negative emissions — Part 2 : Costs , potentials and side effects. Environ. Res. Lett. **12**: 063002. doi:10.1088/1748-9326/aabf9f
Gattuso, J.-P., J.-M. Epitalon, H. Lavigne, and J. Orr. 2021. Seacarb: seawater carbonate chemistry with R. R package version 3.0.
Gattuso, J.-P., A. K. Magnan, L. Bopp, and others. 2018. Ocean Solutions to Address Climate Change and Its Effects on Marine Ecosystems. Front. Mar. Sci. **5**. doi:10.3389/fmars.2018.00337
Gnanadesikan, A., and I. Marinov. 2008. Export is not enough: Nutrient cycling and carbon sequestration. Mar. Ecol. Prog. Ser. **364**: 289–294. doi:10.3354/meps07550
Gnanadesikan, A., J. L. Sarmiento, and R. D. Slater. 2003. Effects of patchy ocean fertilization on atmospheric carbon dioxide and biological production. Global Biogeochem. Cycles **17**: 1–17. doi:10.1029/2002gb001940
Griffies, S. M. 2012. Elements of the Modular Ocean Model (MOM) 2012 Release with Updates.
Guidi, L., L. Stemmann, G. A. Jackson, F. Ibanez, H. Claustre, L. Legendre, M. Picheral, and G. Gorsky. 2009. Effects of phytoplankton community on production, size and export of large aggregates: A world-ocean analysis. Limnol. Oceanogr. **54**: 1951–1963. doi:10.4319/lo.2009.54.6.1951
Harrison, D. P. 2013. A method for estimating the cost to sequester carbon dioxide by delivering iron to the ocean. Int. J. Glob. Warm. **5**: 231–254. doi:10.1504/IJGW.2013.055360
Hauck, J., A. Lenton, C. Langlais, and R. Matear. 2018. The Fate of Carbon and Nutrients Exported Out of the Southern Ocean. Global Biogeochem. Cycles **32**: 1556–1573. doi:10.1029/2018GB005977
He, J., and M. D. Tyka. 2023. Limits and CO2 equilibration of near-coast alkalinity enhancement. Biogeosciences **20**: 27–43. doi:10.5194/bg-20-27-2023
Heuzé, C. 2021. Antarctic Bottom Water and North Atlantic Deep Water in CMIP6 models. Ocean Sci. **17**: 59–90. doi:10.5194/os-17-59-2021
Holte, J., L. D. Talley, J. Gilson, and D. Roemmich. 2017. An Argo mixed layer climatology and database. Geophys. Res. Lett. **44**: 5618–5626. doi:10.1002/2017GL073426

Ito, T., and M. J. Follows. 2005. Preformed phosphate, soft tissue pump and atmospheric CO2. J. Mar. Res. **63**: 813–839. doi:10.1357/0022240054663231
Jin, X., and N. Gruber. 2003. Offsetting the radiative benefit of ocean iron fertilization by enhancing N2O emissions. Geophys. Res. Lett. **30**: 1–4. doi:10.1029/2003GL018458
Katlein, C., S. Arndt, H. J. Belter, G. Castellani, and M. Nicolaus. 2019. Seasonal Evolution of Light Transmission Distributions Through Arctic Sea Ice. J. Geophys. Res. Ocean. **124**: 5418–5435. doi:10.1029/2018JC014833
Katsumata, K., H. Nakano, and Y. Kumamoto. 2015. Dissolved oxygen change and freshening of Antarctic Bottom water along 62°S in the Australian-Antarctic Basin between 1995/1996 and 2012/2013. Deep. Res. Part II Top. Stud. Oceanogr. **114**: 27–38. doi:10.1016/j.dsr2.2014.05.016
Krishnamurthy, A., J. K. Moore, and S. C. Doney. 2008. The effects of dilution and mixed layer depth on deliberate ocean iron fertilization: 1-D simulations of the southern ocean iron experiment (SOFeX). J. Mar. Syst. **71**: 112–130. doi:10.1016/j.jmarsys.2007.07.002
Lampitt, R. S., E. P. Achterberg, T. R. Anderson, and others. 2008. Ocean fertilization: A potential means of geoengineering? Philos. Trans. R. Soc. A Math. Phys. Eng. Sci. **366**: 3919–3945. doi:10.1098/rsta.2008.0139
Large, W. G., and S. G. Yeager. 2009. The global climatology of an interannually varying air - Sea flux data set. Clim. Dyn. **33**: 341–364. doi:10.1007/s00382-008-0441-3
Law, C. S., and R. D. Ling. 2001. Nitrous oxide flux and response to increased iron availability in the Antarctic Circumpolar Current. Deep. Res. Part II Top. Stud. Oceanogr. **48**: 2509–2527. doi:10.1016/S0967-0645(01)00006-6
Lehahn, Y., I. Koren, S. Sharoni, F. D'Ovidio, A. Vardi, and E. Boss. 2017. Dispersion/dilution enhances phytoplankton blooms in low-nutrient waters. Nat. Commun. **8**: 1–8. doi:10.1038/ncomms14868
Marinov, I., A. Gnanadesikan, J. R. Toggweiler, and J. L. Sarmiento. 2006. The Southern Ocean biogeochemical divide. Nature **441**: 964–967. doi:10.1038/nature04883
Marshall, J., and K. Speer. 2012. Closure of the meridional overturning circulation through Southern Ocean upwelling. Nat. Geosci. **5**: 171–180. doi:10.1038/ngeo1391
Martin, J. H. 1990. Glacial-Interglacial CO2 change: the iron hypothesis. Paleoceanography **5**: 1–13.
Martin, J. H., G. a. Knauer, D. M. Karl, and W. W. Broenkow. 1987. VERTEX: carbon cycling in the northeast Pacific. Deep Sea Res. Part A. Oceanogr. Res. Pap. **34**: 267–285. doi:10.1016/0198-0149(87)90086-0
Martínez-García, A., D. M. Sigman, H. Ren, and others. 2014. Iron fertilization of the subantarctic ocean during the last ice age. Science (80-.). **343**: 1347–1350. doi:10.1126/science.1246848
Millero, F. J., T. B. Graham, F. Huang, H. Bustos-Serrano, and D. Pierrot. 2006. Dissociation constants of carbonic acid in seawater as a function of salinity and temperature. Mar. Chem. **100**: 80–94. doi:10.1016/j.marchem.2005.12.001
Mobley, C. D., and E. S. Boss. 2012. Improved irradiances for use in ocean heating, primary production, and photo-oxidation calculations. Appl. Opt. **51**: 6549–6560. doi:10.1364/AO.51.006549
Morrison, A. K., A. M. Hogg, M. H. England, and P. Spence. 2020. Warm Circumpolar Deep Water transport toward Antarctica driven by local dense water export in canyons. Sci. Adv. eaav2516. doi:10.1126/sciadv.aav2516
NASEM. 2021. A Research Strategy for Ocean-based Carbon Dioxide Removal and Sequestration, Doney, Sco.
Nemet, G. F., M. W. Callaghan, F. Creutzig, and others. 2018. Negative emissions — Part 3: Innovation and upscaling. Environ. Res. Lett. **13**: 06300,.
Ohshima, K. I., Y. Fukamachi, G. D. Williams, and others. 2013. Antarctic Bottom Water production by intense sea-ice formation in the Cape Darnley polynya. Nat. Geosci. **6**: 235–240. doi:10.1038/ngeo1738
Orsi, A. H., W. M. Smethie, and J. L. Bullister. 2002. On the total input of Antarctic waters to the deep ocean: A preliminary estimate from chlorofluorocarbon measurements. J. Geophys. Res. Ocean. **107**. doi:10.1029/2001jc000976
Oschlies, A., W. Koeve, W. Rickels, and K. Rehdanz. 2010. Side effects and accounting aspects of hypothetical large-scale Southern Ocean iron fertilization. Biogeosciences **7**: 4014–4035. doi:10.5194/bg-7-4017-2010
Palter, J. B., J. L. Sarmiento, A. Gnanadesikan, J. Simeon, and R. D. Slater. 2010. Fueling export production: Nutrient return pathways from the deep ocean and their dependence on the Meridional Overturning Circulation. Biogeosciences **7**: 3549–3568. doi:10.5194/bg-7-3549-2010
Paris, C. B., J. Helgers, E. van Sebille, and A. Srinivasan. 2013. Connectivity Modeling System: A probabilistic modeling tool for the multi-scale tracking of biotic and abiotic variability in the ocean. Environ. Model. Softw. **42**: 47–54. doi:10.1016/j.envsoft.2012.12.006
Primeau, F. W., M. Holzer, and T. DeVries. 2013. Southern Ocean nutrient trapping and the efficiency of the biological pump. J. Geophys. Res. Ocean. **118**: 2547–2564. doi:10.1002/jgrc.20181

Prytherch, J., I. Brooks, P. Crill, and others. 2017. Direct determination of the air-sea CO2 gas transfer velocity in Arctic sea ice regions. Geophys. Res. Lett. **44**: 3770–3778. doi:10.1002/2017GL073593
Rickels, W., K. Rehdanz, and A. Oschlies. 2012. Economic prospects of ocean iron fertilization in an international carbon market. Resour. Energy Econ. **34**: 129–150. doi:10.1016/j.reseneeco.2011.04.003
Robinson, J., E. E. Popova, A. Yool, M. Srokosz, R. S. Lampitt, and J. R. Blundell. 2014. How deep is deep enough? Ocean iron fertilization and carbon sequestration in the Southern Ocean. Geophys. Res. Lett. **41**: 2489–2495. doi:10.1002/2013GL058799
Rogelj, J., D. Shindell, K. Jiang, and others. 2018. Mitigation Pathways Compatible with 1.5°C in the Context of Sustainable Development, p. 93–174. *In* V. Masson-Delmotte, P. Zhai, H.O. Poertner, et al. [eds.], Global Warming of 1.5°C. An IPCC Special Report on the impacts of global warming of 1.5°C above pre-industrial levels and related global greenhouse gas emission pathways, in the context of strengthening the global response to the threat of climate change,.
Rohr, T. 2019. Southern Ocean Iron Fertilization : An Argument Against Commercialization but for Continued Research Amidst Lingering Uncertainty. J. Sci. Policy Gov. **15**.
Ruseva, T., J. Hedrick, G. Marland, H. Tovar, C. Sabou, and E. Besombes. 2020. Rethinking standards of permanence for terrestrial and coastal carbon: implications for governance and sustainability. Curr. Opin. Environ. Sustain. **45**: 69–77. doi:10.1016/j.cosust.2020.09.009
Sarmiento, J. L., and N. Gruber. 2006. Ocean biogeochemical dynamics, Princeton University Press.
Sarmiento, J. L., and J. C. Orr. 1991. Three-dimensional simulations of the impact of Southern Ocean nutrient depletion on atmospheric CO2 and ocean chemistry. Limnol. Oceanogr. **36**: 1928–1950. doi:10.4319/lo.1991.36.8.1928
Sarmiento, J. L., R. D. Slater, J. Dunne, A. Gnanadesikan, and M. R. Hiscock. 2010. Efficiency of small scale carbon mitigation by patch iron fertilization. Biogeosciences **7**: 3593–3624. doi:10.5194/bg-7-3593-2010
Siegel, D. A., T. Devries, S. C. Doney, and T. Bell. 2021. Assessing the sequestration time scales of some ocean-based carbon dioxide reduction strategies. Environ. Res. Lett. **16**. doi:10.1088/1748-9326/ac0be0
Smetacek, V., C. Klaas, V. H. Strass, and others. 2012. Deep carbon export from a Southern Ocean iron-fertilized diatom bloom. Nature **487**: 313–319. doi:10.1038/nature11229
Strong, A., S. Chisholm, C. Miller, and J. Cullen. 2009. Ocean fertilization: Time to move on. Nature **461**: 347–348. doi:10.1038/461347a
Tagliabue, A., T. Mtshali, O. Aumont, A. R. Bowie, M. B. Klunder, A. N. Roychoudhury, and S. Swart. 2012. A global compilation of dissolved iron measurements: Focus on distributions and processes in the Southern Ocean. Biogeosciences **9**: 2333–2349. doi:10.5194/bg-9-2333-2012
Tamsitt, V., H. F. Drake, A. K. Morrison, and others. 2017. Spiraling pathways of global deep waters to the surface of the Southern Ocean. Nat. Commun. **8**: 1–10. doi:10.1038/s41467-017-00197-0
The Royal Society. 2009. Geoengineering the climate: Science, Governance and Uncertainty Report No. RS1636.
Twining, B. S., S. B. Baines, N. S. Fisher, and M. R. Landry. 2004. Cellular iron contents of plankton during the Southern Ocean Iron Experiment (SOFeX). Deep. Res. Part I Oceanogr. Res. Pap. **51**: 1827–1850. doi:10.1016/j.dsr.2004.08.007
Venables, H., and C. M. Moore. 2010. Phytoplankton and light limitation in the Southern Ocean: Learning from high-nutrient, high-chlorophyll areas. J. Geophys. Res. **115**. doi:10.1029/2009jc005361
Wanninkhof, R. 2014. Relationship between wind speed and gas exchange over the ocean revisited. Limnol. Oceanogr. Methods **12**: 351–362. doi:10.4319/lom.2014.12.351
Wassmann, P. 1998. Retention versus export food chains: Processes controlling sinking loss from marine pelagic systems. Hydrobiologia **363**: 29–57. doi:10.1023/A:1003113403096
Williams, G. D., S. Aoki, S. S. Jacobs, S. R. Rintoul, T. Tamura, and N. L. Bindoff. 2010. Antarctic bottom water from the adélie and George v Land Coast, East Antarctica (140-149°E). J. Geophys. Res. Ocean. **115**: 1–29. doi:10.1029/2009JC005812
Williamson, P., D. W. R. Wallace, C. S. Law, and others. 2012. Ocean fertilization for geoengineering: A review of effectiveness, environmental impacts and emerging governance. Process Saf. Environ. Prot. **90**: 475–488. doi:10.1016/j.psep.2012.10.007
Xie, Y., V. Tamsitt, and L. T. Bach. 2022. Localizing the Southern Ocean Biogeochemical Divide. Geophys. Res. Lett. **49**: 1–9. doi:10.1029/2022GL098260
Yoon, J. E., K. C. Yoo, A. M. MacDonald, and others. 2018. Reviews and syntheses: Ocean iron fertilization experiments - Past, present, and future looking to a future Korean Iron Fertilization Experiment in the Southern Ocean (KIFES) project. Biogeosciences **15**: 5847–5889. doi:10.5194/bg-15-5847-2018
Zahariev, K., J. R. Christian, and K. L. Denman. 2008. Preindustrial, historical, and fertilization simulations using a

global ocean carbon model with new parameterizations of iron limitation, calcification, and N2 fixation. Prog. Oceanogr. **77**: 56–82. doi:10.1016/j.pocean.2008.01.007

Figure 1.

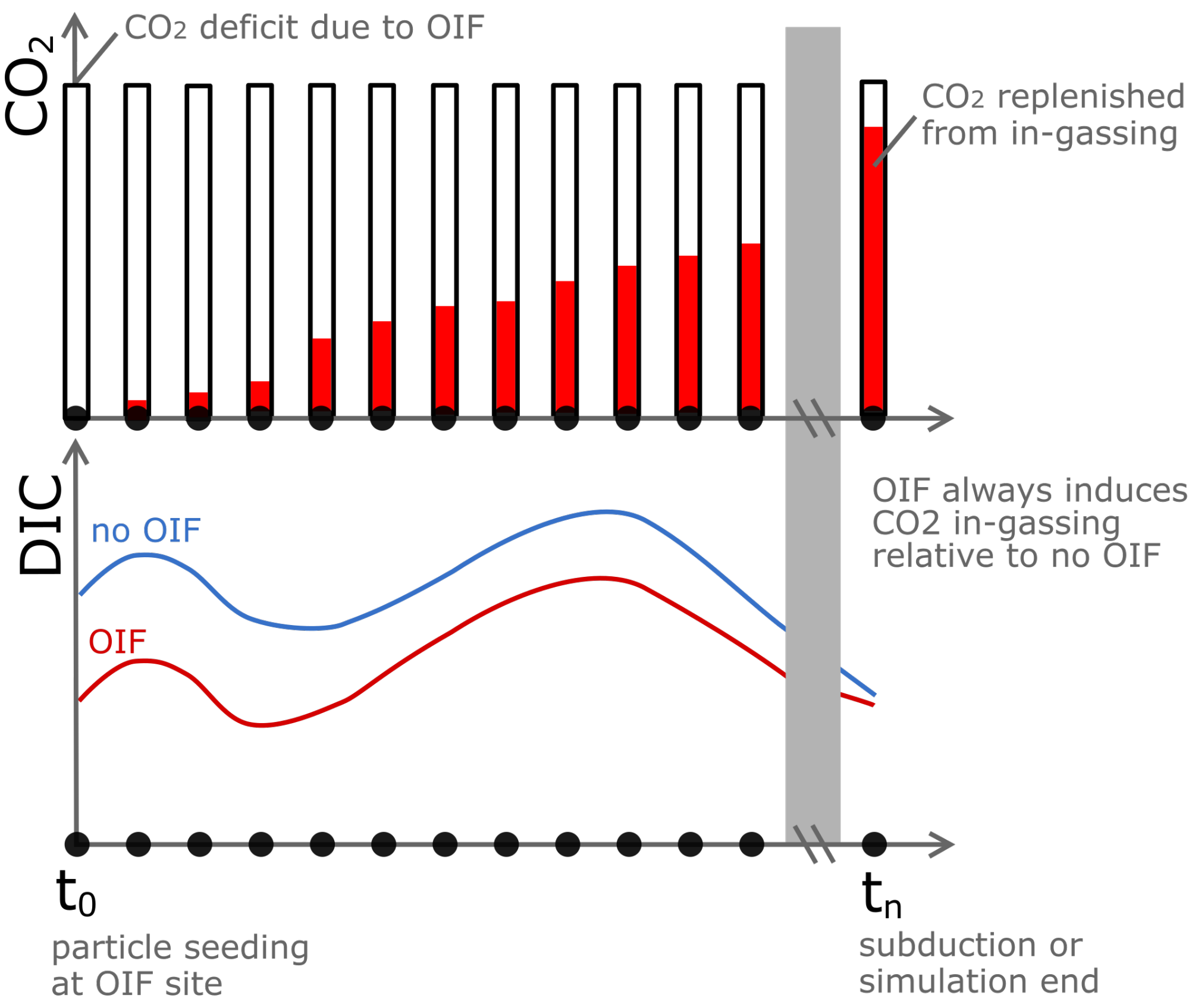
CO2
CO2 deficit due to OIF
CO2 replenished from in-gassing
DIC
no OIF
OIF
OIF always induces CO2 in-gassing relative to no OIF
t0
particle seeding at OIF site
tn
subduction or simulation end

Figure 2.

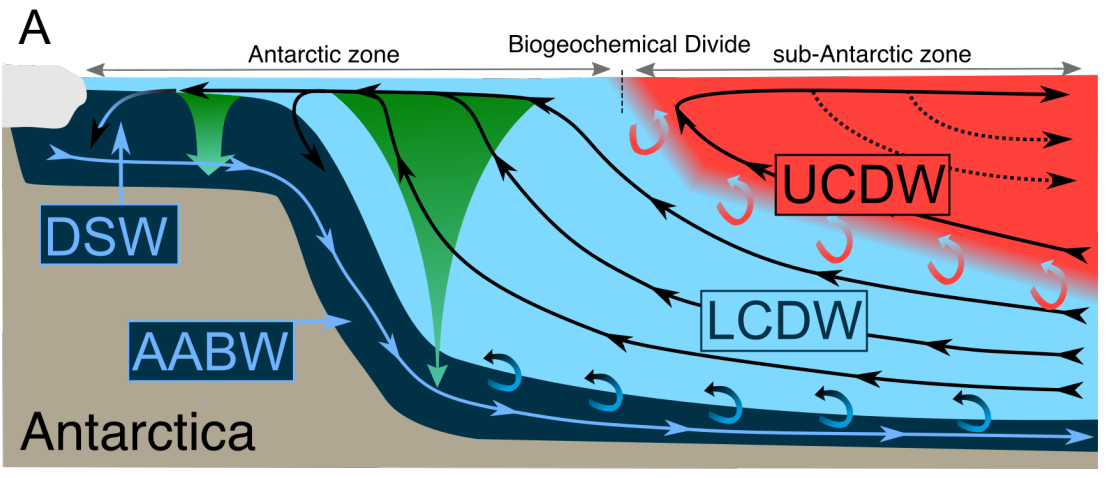
A
Antarctic zone
Biogeochemical Divide
sub-Antarctic zone
UCDW
DSW
LCDW
AABW
Antarctica

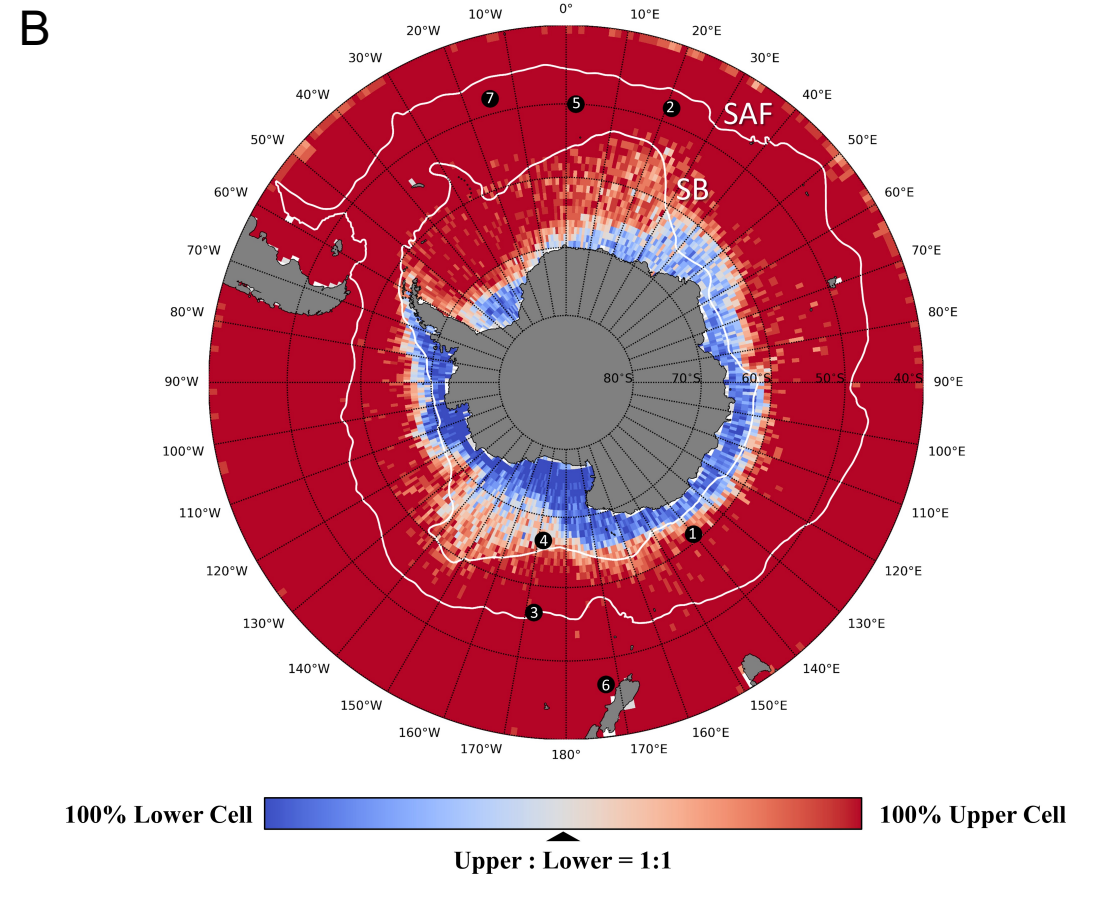
B
SAF
SB
0°
10°W
10°E
20°W
20°E
30°W
30°E
40°W
40°E
50°W
50°E
60°W
60°E
70°W
70°E
80°W
80°E
90°W
90°E
100°W
100°E
110°W
110°E
120°W
120°E
130°W
130°E
140°W
140°E
150°W
150°E
160°W
160°E
170°W
170°E
180°
80°S
70°S
60°S
50°S
40°S
1
2
3
4
5
6
7
100% Lower Cell
100% Upper Cell
Upper : Lower = 1:1

Figure 3.

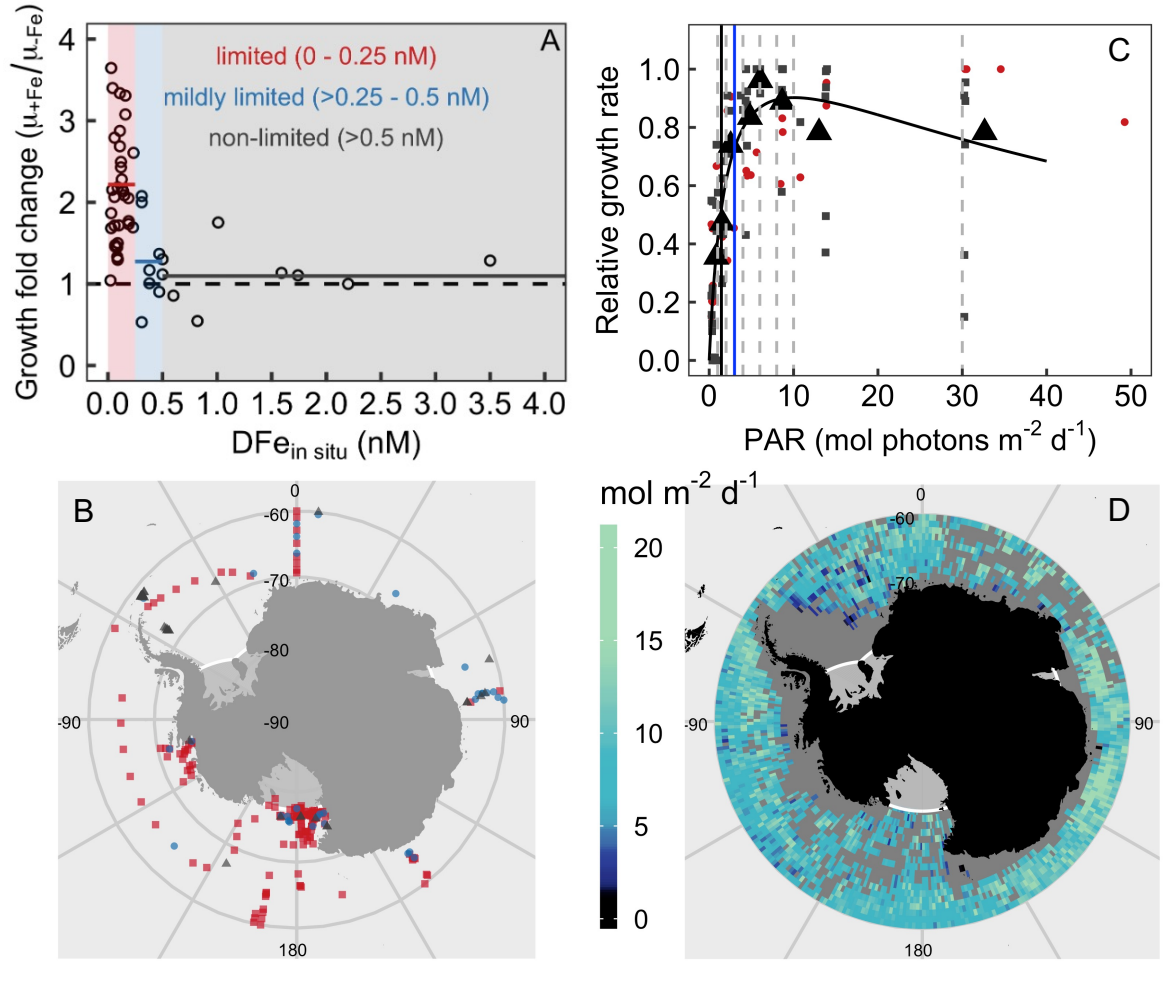
A
limited (0 - 0.25 nM)
mildly limited (>0.25 - 0.5 nM)
non-limited (>0.5 nM)
Growth fold change (μ+Fe/μ-Fe)
DFe in situ (nM)
C
Relative growth rate
PAR (mol photons m-2 d-1)
B
D
mol m-2 d-1

Figure 4.

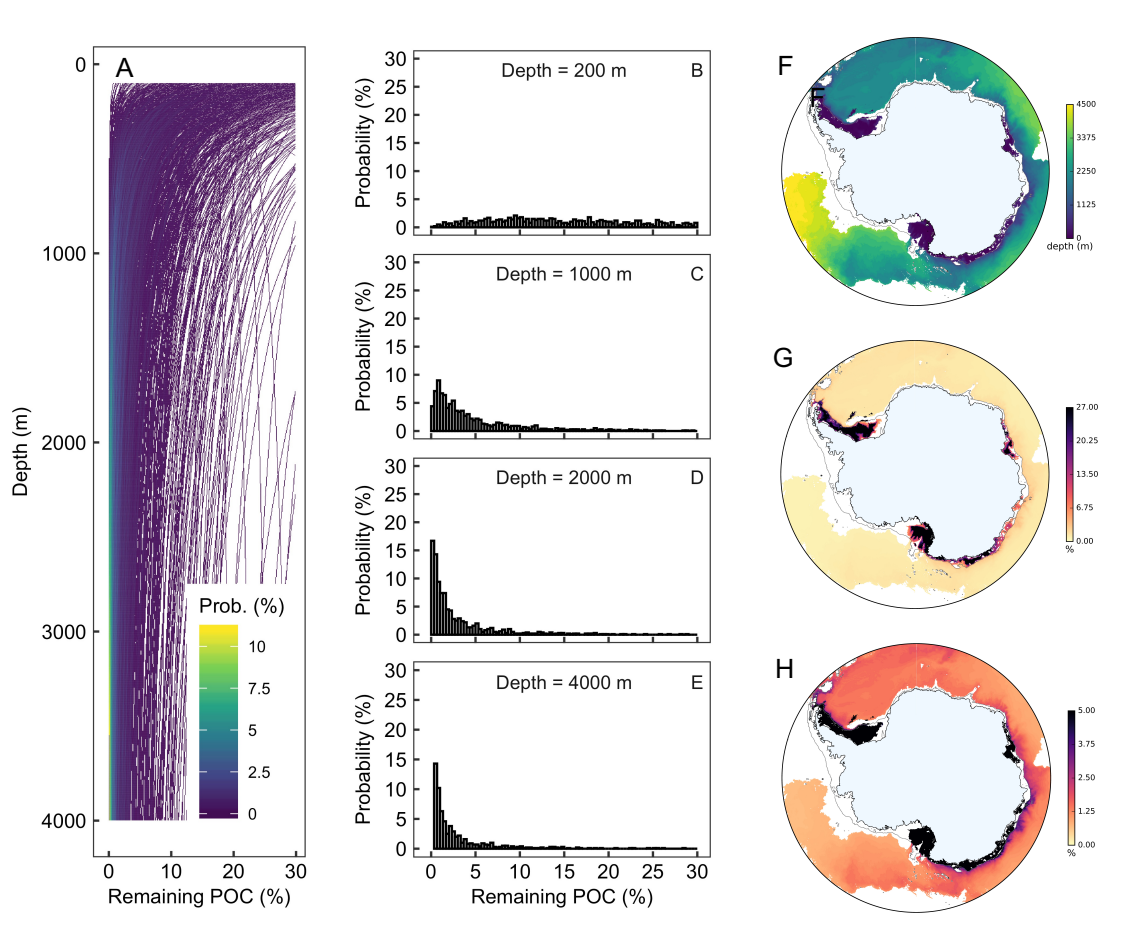
A
Depth (m)
0
1000
2000
3000
4000
Prob. (%)
10
7.5
5
2.5
0
0
10
20
30
Remaining POC (%)
B
Depth = 200 m
C
Depth = 1000 m
D
Depth = 2000 m
E
Depth = 4000 m
Probability (%)
0
5
10
15
20
25
30
Remaining POC (%)
F
4500
3375
2250
1125
0
depth (m)
G
27.00
20.25
13.50
6.75
0.00
%
H
5.00
3.75
2.50
1.25
0.00
%

Figure 5.

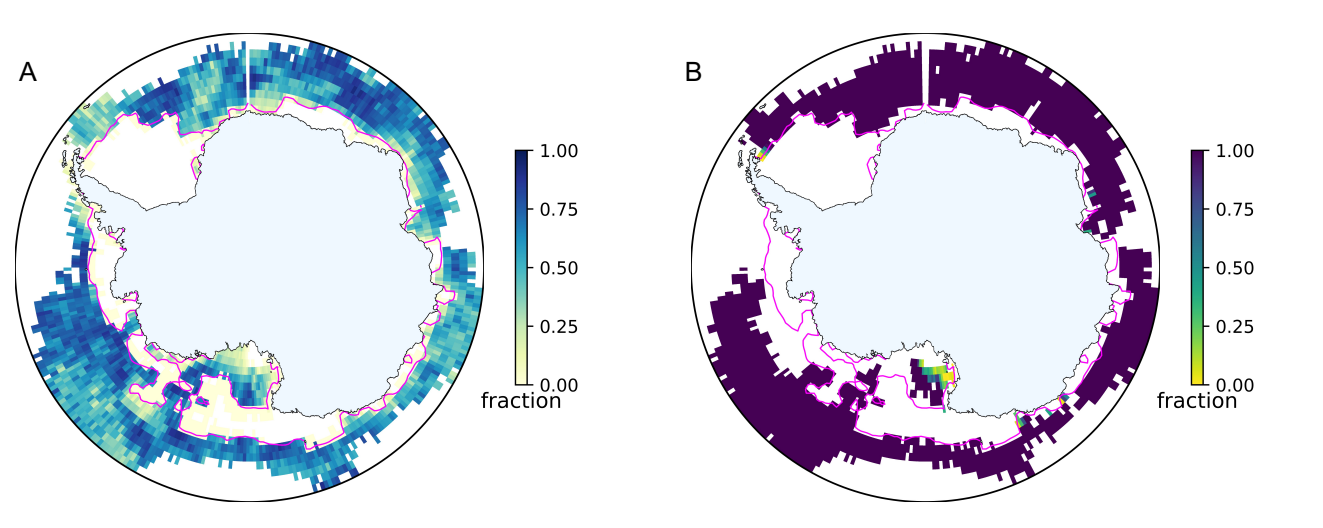
A
1.00
0.75
0.50
0.25
0.00
fraction
B
1.00
0.75
0.50
0.25
0.00
fraction

Figure 6.

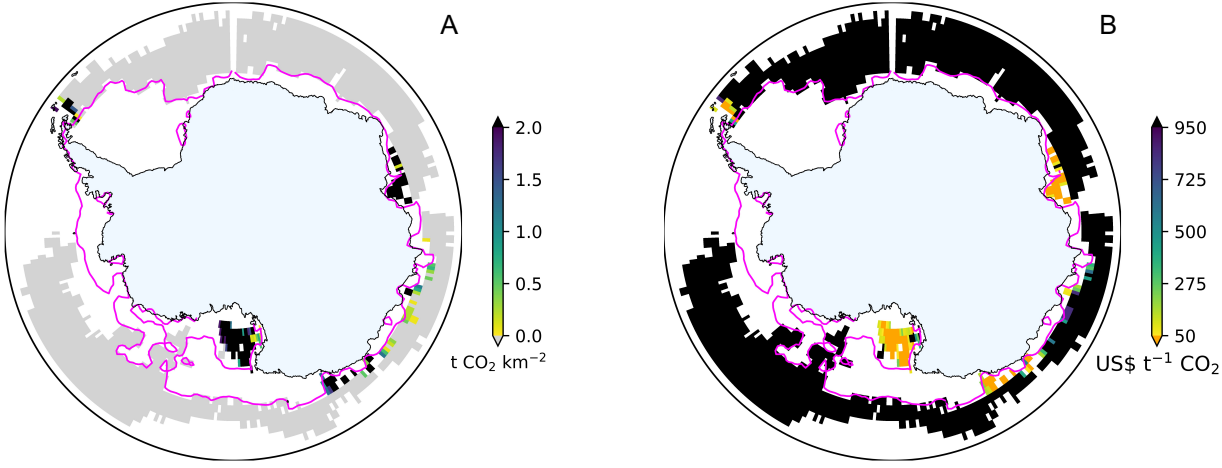
A
2.0
1.5
1.0
0.5
0.0
t CO2 km−2
B
950
725
500
275
50
US$ t−1 CO2

Figure 7.

All
$O_{transport}$
fN_2O
POC_{AABW}
C/Fe
A
-10 0 10 20 30 40 50
CDR (t CO_2 km^{-2})
All
$O_{transport}$
fN_2O
POC_{AABW}
C/Fe
depth
200m
1000m
B
-10 0 10 20 30 40 50
CDR (t CO_2 km^{-2})
98% between 0-100 US Dollar at 200 m
27% between 0-100 US Dollar at 1000 m
Probability (%)
C
0 100 200 300 400
Costs (US Dollar t^{-1} CO_2)
86% between 0-100 US Dollar at 200 m
12% between 0-100 US Dollar at 1000 m
Probability (%)
D
0 100 200 300 400
Costs (US Dollar t^{-1} CO_2)

Figure 8.

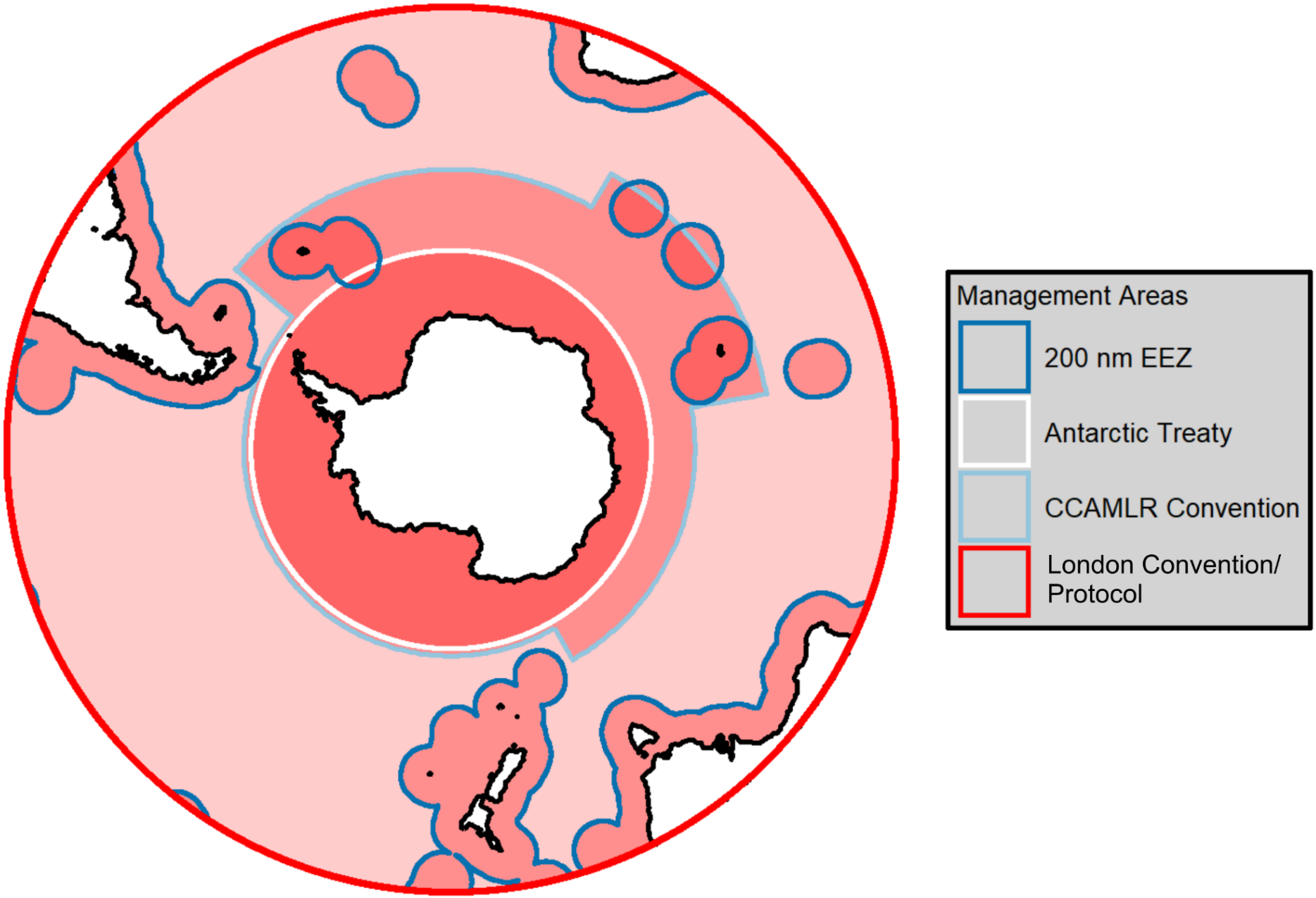
Management Areas
200 nm EEZ
Antarctic Treaty
CCAMLR Convention
London Convention/
Protocol